Click Here for Full Article

Plio-Quaternary exhumation history of the central Nepalese Himalaya:
2. Thermokinematic and thermochronometer age prediction model

David M. Whipp Jr.,[1] Todd A. Ehlers,[1] Ann E. Blythe,[2,3] Katharine W. Huntington,[4,5] Kip V. Hodges,[4,6] Douglas W. Burbank[7]

[1] In the Himalaya and other active convergent orogens, linear relationships between thermochronometer sample age and elevation are often used to estimate long-term exhumation rates. In these regions, high-relief topography and nonvertical exhumation pathways may invalidate such one-dimensional (1-D) interpretations and lead to significant errors. To quantify these errors, we integrate apatite fission track (AFT) ages from the central Himalaya with a 3-D coupled thermokinematic model, from which sample cooling ages are predicted using a cooling-rate-dependent algorithm. By changing the slip partitioning between faults near the Main Central thrust and the Main Frontal thrust system at the Himalayan range front, we are able to explore the significance of different tectonic scenarios on predicted thermochronometer ages. We find that the predicted AFT cooling ages are not sensitive to the different slip partitioning scenarios but depend strongly on erosion rate: Predicted ages are most consistent with kinematic models that produce erosion rates of 1.8–5.0 mm/yr. This range is considerably smaller than that derived from regression lines through the data (−2.6–12.2 mm/yr). The pattern of observed AFT ages shows more complexity than our models predict. None of the kinematic scenarios are able to fit >80% of all of the AFT data, most likely because erosion is spatially variable. Such complexities notwithstanding, we conclude that the use of thermokinematic modeling and thermochronologic data sets to explore detailed fault kinematics in rapidly eroding active orogens has great promise but requires integration of higher-temperature (>∼350°C) data sets to maximize effectiveness. **Citation:** Whipp, D. M., Jr., T. A. Ehlers, A. E. Blythe, K. W. Huntington, K. V. Hodges, and D. W. Burbank (2007), Plio-Quaternary exhumation history of the central Nepalese Himalaya: 2. Thermokinematic and thermochronometer age prediction model, *Tectonics*, *26*, TC3003, doi:10.1029/2006TC001991.

1. Introduction

[2] Climate-driven erosion has been hypothesized to drive deformation along the Himalayan front [*Beaumont et al.*, 2001; *Hodges et al.*, 2001, 2004; *Thiede et al.*, 2004]. Detailed studies that quantify long-term erosion rates are therefore needed as a first step toward calibrating geodynamic and landform evolution models where erosional processes are coupled with deformation [e.g., *Beaumont et al.*, 1992; *Willett*, 1999]. In some orogens, zones of high precipitation have been suggested to correspond with regions of enhanced long-term erosion rates [e.g., *Reiners et al.*, 2003]; however, in the Himalaya, increased erosion rates have also been argued to be decoupled from climate forcing [e.g., *Burbank et al.*, 2003] and the extent of climate-erosion coupling has been shown to vary temporally [e.g., *Thiede et al.*, 2004, 2005]. An ideal location to address some of these issues is the central Nepalese Himalaya (Figure 1a), where the late Cenozoic uplift of the Tibetan Plateau may have significantly increased the strength of the Indian Monsoon. This strengthening could have increased precipitation and potentially focused erosion on the southern margin of the plateau [*Molnar et al.*, 1993; *Ruddiman et al.*, 1997]. When combined with evidence of late Miocene–Quaternary renewal of faulting within the interior of the Himalayan orogenic wedge [*Seeber and Gornitz*, 1983; *Macfarlane et al.*, 1992; *Harrison et al.*, 1997; *Catlos et al.*, 2001; *Hodges et al.*, 2004; *Wobus et al.*, 2005], the timing of the hypothesized increase in erosion suggests that climate-driven erosion may have induced tectonic activity through modification of gravitational body forces. The objective of this study is to take an initial step toward testing the previous hypothesis by quantifying the rates and spatial variations in erosion across a drainage basin within the Himalayan front.

[3] In general, the major south vergent structures in the Himalaya developed through sequential activation of faults south of the previous deformation front [e.g., *Hodges*,

[1]Department of Geological Sciences, University of Michigan, Ann Arbor, Michigan, USA.

[2]Department of Earth Sciences, University of Southern California, Los Angeles, California, USA.

[3]Now at Geology Department, Occidental College, Los Angeles, California, USA.

[4]Department of Earth, Atmospheric and Planetary Sciences, Massachusetts Institute of Technology, Cambridge, Massachusetts, USA.

[5]Now at Division of Geological and Planetary Sciences, California Institute of Technology, Pasadena, California, USA.

[6]Now at School of Earth and Space Exploration, Arizona State University, Tempe, Arizona, USA.

[7]Department of Earth Science, University of California, Santa Barbara, Santa Barbara, California, USA.
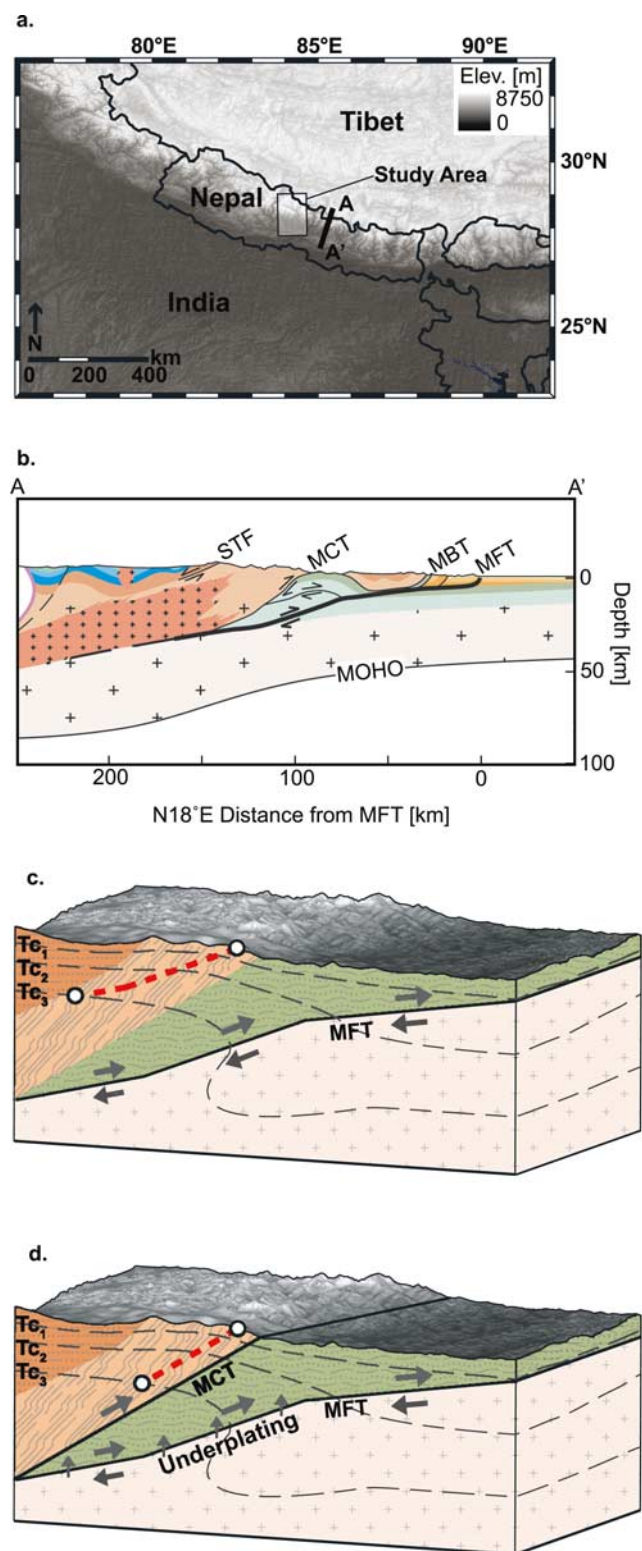
2000]. As a new fault in a more distal position is initiated, slip along more hinterland faults is commonly thought to have ceased. *Lavé and Avouac* [2000] suggest that nearly all of the Holocene convergence between India and southern Tibet has been accommodated by the young range-bounding fault, the Main Frontal thrust (MFT): an observation that could be consistent with slip solely on the most distal fault. However, thermochronologic, geomorphic, and cosmogenic isotope evidence support the idea that faulting may occur out of sequence near the Main Central thrust (MCT) and within its proximal footwall (1–30 km). For example, within the interior of the Himalayan wedge, faults near the MCT trace may have been active during the late Miocene and Pliocene, and could be active today [*Wobus et al.*, 2003; *Hodges et al.*, 2004; *Wobus et al.*, 2005]. Very young cooling ages and cosmogenic nuclide data for samples collected from within the MCT hanging wall suggest erosion at average rates of ∼1–3 mm/yr since the Pliocene [*Burbank et al.*, 2003; *Vance et al.*, 2003; *Thiede et al.*, 2004; *Niemi et al.*, 2005]. *Burbank et al.* [2003] reported uniformly young apatite fission track (AFT) cooling ages in the hanging wall of the MCT in the Annapurna Himalaya of central Nepal, a region in which precipitation is spatially variable from ∼0.5–4.0 m/yr. As a consequence, they found no evidence of a close coupling of precipitation with rapid exhumation in central Nepal. However, the mean annual precipitation records and average exhumation rates differ in timescale by several orders of magnitude, so direct a comparison may have limited utility. In NW India, *Thiede et al.* [2004, 2005] found their youngest white mica $^{40}Ar/^{39}Ar$ cooling ages within the hanging wall of the Munsiari thrust. The Munsiari thrust is generally not recognized in Nepal, but occupies a structural position beneath the Vaikrita thrust, a fault that most researchers correlate with the MCT in central Nepal [*Valdiya*, 1980]. Conversely, the AFT data of *Thiede et al.* [2004, 2005] were youngest within areas of locally heavy precipitation, suggesting a coupling of climate and erosion over the time during which their AFT samples cooled. *Hodges et al.* [2004] found that

Figure 1. (a) Shaded relief digital elevation model (DEM) of the Himalaya showing the central Nepal study area (rectangle) and the location of (b) a geologic cross section (thick line), modified from Figure 2 of *Lavé and Avouac* [2000]. STF, South Tibetan fault; MCT, Main Central thrust; MBT, Main Boundary thrust; MFT, Main Frontal thrust. (c) Three-dimensional schematic block diagram for tectonic scenario a, where slip occurs only on the MFT (arrows show sense of motion on fault). The exhumation pathway (thick dashed line) would parallel the fault and transport rock through closure temperatures ($Tc_1 - Tc_3$) for several isotopic systems (thin dashed lines). Example exhumation pathway for a thermochronometer sample sensitive to closure temperatures $Tc_1 - Tc_3$ (white circles). (d) Tectonic scenarios b–d, where slip is partitioned between the MCT and MFT. In these scenarios, sample exhumation parallels the MCT and material is transferred into the overriding wedge via underplating (small vertical arrows).
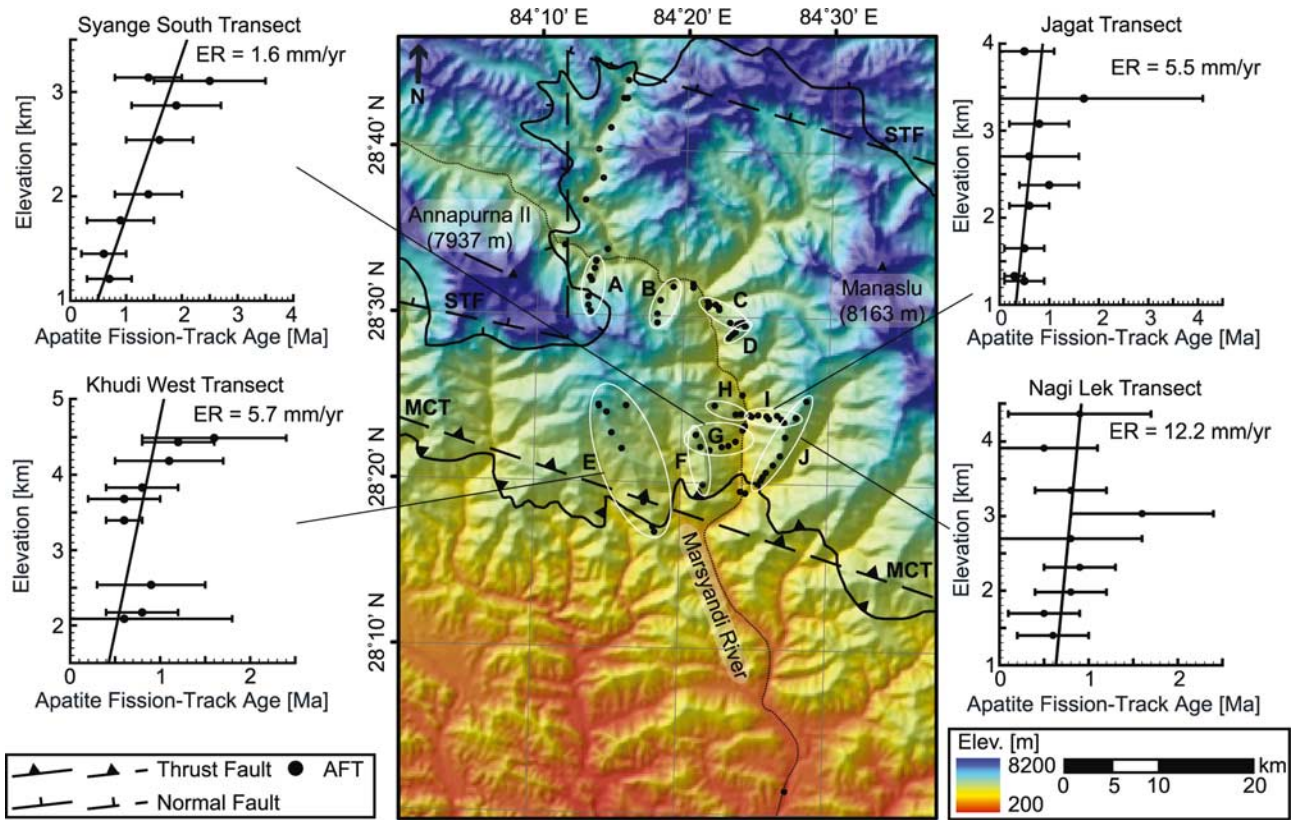
Figure 2. Shaded relief DEM of the Marsyandi River valley, central Nepal showing the surface traces of the STF and MCT II from *Searle and Godin* [2003] (thick solid lines) with the model approximations of those faults (thick dashed lines). Abbreviations are as in Figure 1. Apatite fission track (AFT) sample locations (black circles) are divided into transects (white ovals), where A, Chame; B, Bagarchhap; C, Dharapani; D, Tal; E, Khudi West; F, Khudi East; G, Syange South; H, Syange North; I, Jagat; and J, Nagi Lek. Age-elevation plots are shown for several transects with weighted least squares regression lines showing the range of apparent exhumation rates (ER; 1.6–12.2 mm/yr).

not only were young AFT cooling ages correlated with locally heavy precipitation, but they observed evidence of Quaternary faulting near the MCT in central Nepal. Their observations support theory-based models involving a coupling between erosion along the Himalayan range front and southward extrusion of middle to lower crustal material [*Beaumont et al.*, 2001; *Hodges et al.*, 2001].

[4] Thermochronometer data used by *Burbank et al.* [2003], *Thiede et al.* [2004, 2005] and *Hodges et al.* [2004] record the cooling history of exhumed samples, but the interpretation of cooling ages from an active orogen is not simple. For example, the apparent exhumation rates derived from the slope of AFT cooling ages versus sample elevation [*Thiede et al.*, 2004; *Blythe et al.*, 2007] rely on simplifying assumptions about the subsurface thermal field and exhumation history. In some cases, these assumptions can introduce large (20–200%) errors in the interpreted exhumation rates [*Stüwe et al.*, 1994; *Mancktelow and Grasemann*, 1997; *Ehlers*, 2005]. True exhumation rates can be better constrained using thermokinematic modeling to simulate more realistic subsurface thermal fields and thermal histories of the thermochronometer samples [*Batt*

and Brandon, 2002; *Ehlers et al.*, 2003; *Braun and Robert*, 2005]. Previous thermal and kinematic modeling studies of the Himalaya have approximated the exhumation pathways and the resulting thermal field as two-dimensional with slip on only one fault [*Henry et al.*, 1997; *Bollinger et al.*, 2006; *Brewer and Burbank*, 2006]. Using a two-dimensional (2-D) approximation neglects the three-dimensional (3-D) influence of topography and fault geometry, which can be significant at high slip rates.

[5] In this study, we use a 3-D thermokinematic model of the central Nepalese Himalaya (Figure 1) to predict thermochronometer cooling ages that are compared to a large data set of AFT ages (Figure 2). The AFT data are presented and discussed in detail in the companion paper by *Blythe et al.* [2007]. The primary goal of this study is to use the model to quantify average erosion rates over the time span of AFT ages. A secondary goal is to determine whether the cooling age data can be used to differentiate among various tectonic models. We explore four tectonic scenarios in which Indo-Tibetan convergence is partitioned between the MFT and MCT (Figures 1c and 1d). The model uses fault kinematics and geometries that vary in three dimensions and accounts

for the first-order influence of topography (e.g., valley and ridge positions), which will influence the predicted sample cooling ages. We investigate exhumation and faulting histories of the late Pliocene to Quaternary times, the age range of available AFT data [*Blythe et al.*, 2007]. By comparing the ages predicted from the 3-D thermal model to the data, we are able to quantify potential errors in exhumation rates derived from regression line slopes of sample age versus elevation and infer spatial variations in the erosion history of the central Nepalese Himalaya. Also, by varying overthrusting rates on the MCT and MFT, we address the utility (or lack thereof) of low-temperature thermochronometer data for determining the magnitude of out-of-sequence thrusting in a rapidly eroding region.

2. Geologic Setting

[6] The spectacular peaks of the Himalaya mark the southern margin of a broad region of deformation developed in response to the collision and continued convergence between India and Eurasia since the early Paleogene (∼65–50 Ma) (see reviews by *Gansser* [1964], *Le Fort* [1975], and *Hodges* [2000]). The range is typically divided into four tectonostratigraphic zones: the Tibetan zone, Greater Himalayan zone, the Lesser Himalayan zone and the Subhimalayan zone (terminology of *Hodges* [2000]). Zone contacts correspond to major fault zones that can be traced along strike for much of the length of the orogen. The Paleozoic to Paleogene primarily marine sedimentary rocks of the Tibetan sequence (TS) are bounded on the north by the Indus-Tsangpo suture zone and on the south by low-angle, predominantly normal faults of the South Tibetan fault system (STF). Structurally beneath the TS are metamorphic and igneous rocks of the Greater Himalayan sequence (GHS), which are bounded by the MCT to the south. The dominantly clastic metasedimentary rocks of the Lesser Himalayan sequence (LHS) are bounded to the south by the Main Boundary thrust (MBT). The Subhimalayan zone comprises Neogene and younger foreland basin sediments in the hanging wall of the MFT.

[7] Since the early Miocene, much of the postcollisional convergence between India and Eurasia has been accommodated by a series of southward vergent, southward younging thrust systems. The oldest of these, the Main Central thrust system, developed and experienced its principal movement in latest Oligocene–early Miocene time [*Hubbard and Harrison*, 1989; *Hodges et al.*, 1996; *Coleman*, 1998]. The structurally highest portions of the Lesser Himalayan zone, directly beneath the main splay of the MCT zone, have experienced a complex deformation history related to post-early Miocene southward thrusting. Some of this structure is likely to be related to MCT slip, but other studies [e.g., *DeCelles et al.*, 2001; *Robinson et al.*, 2003; *Pearson and DeCelles*, 2005] have argued convincingly that most slip can be attributed to Middle Miocene development of the Ramgarh thrust and a Lesser Himalayan duplex system as deformation stepped progressively southward into the Lesser Himalayan zone. The principal locus of surface shortening is generally thought to have shifted to the MBT and, eventually, to the MFT zones in late Miocene-Pliocene time [e.g., *Hodges*, 2000, and references therein]. Most researchers regard the MFT as projecting downdip, across a buried ramp beneath the Lesser Himalaya–Greater Himalayan zone transition, to connect with a master décollement referred to as the Main Himalayan thrust (MHT) [e.g., *Lyon-Caen and Molnar*, 1983; *Schelling and Arita*, 1991; *Pandey et al.*, 1995].

[8] Despite this general southward progression of thrust deformation, several studies have yielded convincing evidence of significant out-of-sequence thrusting over the early Miocene–Recent interval [*Brun et al.*, 1985; *Grujic et al.*, 1996; *Hodges et al.*, 1996; *Searle*, 1999]. Of particular interest to our study is the evidence for very young out-of-sequence thrusting near the trace of the MCT system and within the northernmost Lesser Himalayan zone. *Seeber and Gornitz* [1983] first suggested the possibility of out-of-sequence thrusting along the MCT trace based on an analysis of river profiles as they crossed the Greater Himalayan–Lesser Himalayan zone boundary. Subsequently, very young ^{40}Ar/^{39}Ar cooling ages from rocks at this structural level were attributed to late stage reactivation of the MCT system by *Macfarlane* [1993], although both *Copeland et al.* [1991] and *Edwards* [1995] suggested an alternative interpretation based on the possibility of hydrothermal resetting. The documentation by *Harrison et al.* [1997] and *Catlos et al.* [2001] of late Miocene–Pliocene metamorphic monazite growth during deformation at this level renewed the argument for out-of-sequence thrusting, but some of the strongest evidence in favor of this process comes from integrated structural, geomorphic, and thermochronologic studies in central Nepal [*Wobus et al.*, 2003; *Hodges et al.*, 2004; *Wobus et al.*, 2005; *Huntington and Hodges*, 2006]. These findings show that brittle thrust structures within a few kilometers of the outcrop trace of the principal strand of the MCT system have experienced slip in late Pliocene–Quaternary time and, as a consequence, separate domains with distinctive patterns of mineral cooling ages and Quaternary exhumation histories. Evidence for Quaternary out-of-sequence faulting, however, conflicts with the work of *Lavé and Avouac* [2000] who suggest little to no out-of-sequence thrusting has occurred during the Holocene. This conflict shows that the magnitude of post-late Miocene out-of-sequence thrusting is unclear. If there has been a significant amount of out-of-sequence thrusting, presumably this shortening is transferred downdip to the MHT where the out-of-sequence structures splay off of that master décollement [*Hodges et al.*, 2001].

3. Thermochronometer Data Set

[9] Thermochronometer ages yield the time since samples cooled below their effective closure temperature [*Dodson*, 1973]. When combined with estimates of the distance traveled from the closure temperature isotherm to the surface, the data provide a means for determining long-term (>10^5 years) exhumation rates. Higher-temperature thermochronometers have closure temperatures at greater depths, thus the exhumation rates calculated from those

systems integrate over longer time periods and greater distances. Lower-temperature AFT data are used here to quantify rock exhumation histories. For comparison to other data sets, higher-temperature muscovite ^{40}Ar/^{39}Ar ages are predicted from the thermokinematic model discussed below. AFT cooling ages are calculated using the density of damage trails created by spontaneous fission of ^{238}U at a known rate that are preserved within the crystal lattice of apatite in a rock sample (see reviews by *Donelick et al.* [2005] and *Tagami and O'Sullivan* [2005]). Muscovite ^{40}Ar/^{39}Ar cooling ages are based on measuring the retention of ^{40}Ar derived from the natural decay of ^{40}K in muscovite (see review by *Harrison and Zeitler* [2005]). Apatite fission track and muscovite ^{40}Ar/^{39}Ar cooling ages have cooling-rate-dependent closure temperatures of $\sim$100–140°C and $\sim$350–425°C, respectively, for cooling rates of 2–100°C/Myr [*Robbins*, 1972; *Hames and Bowring*, 1994; *Donelick et al.*, 2005; *Ehlers et al.*, 2005; *Tagami and O'Sullivan*, 2005].

[10] *Blythe et al.* [2007] provide bedrock AFT cooling ages that present a detailed exhumation history for the Marsyandi River catchment in central Nepal. We use 82 AFT ages reported by *Blythe et al.* [2007] to compare to ages predicted from a thermokinematic model. The AFT data are divided into ten transects to aid in observing any spatial variations in exhumation (Figure 2). We briefly summarize the data used here, and the reader is referred to *Blythe et al.* [2007] for a more thorough discussion.

[11] The AFT sample ages range from ≤0.4 (95% confidence interval) to 3.8 ± 1.0 Ma (2σ uncertainty) across the study region and samples span an elevation range of 474–4621 m. There is no clear trend in the spatial distribution of ages across the study area, although very young ages (<0.5 Ma) tend to occur at low elevation, near the rivers. The simplest way to get an estimate of exhumation rates from data collected in vertical transects is to plot the sample ages as a function of elevation [*Wagner and Reimer*, 1972; *Wagner et al.*, 1977], where the slope of a regression line through the data is the apparent exhumation rate. Although these transects are not strictly vertical, age-elevation regressions can be carried out and the range of apparent exhumation rates from the slope of a weighted least squares regression of each transect are highly variable. The apparent rates range between −12.1 and 12.2 mm/yr, where negative rates are from transects with inverted age-elevation trends.

4. The Model

[12] Although calculating exhumation rates from regression lines on age-elevation plots is a common way to interpret data, large uncertainties are possible when samples are collected over a horizontal distance that is greater than the wavelength over which topography affects the subsurface closure isotherm geometry. Additional problems are possible if the samples are carried in a thrust sheet with a large lateral component of motion, where nonvertical transport can lead to additional uncertainty. To avoid these uncertainties, it is useful to estimate the distance a sample has traveled since passing through the closure temperature

for that system. In the simplest case, that distance can be determined by calculating a steady state one-dimensional (1-D) vertical thermal profile or using a constant geothermal gradient. Assuming vertical sample exhumation, the exhumation rate is calculated by measuring the distance from the surface to the closure temperature isotherm and dividing that distance by the sample age. In active orogens, however, the thermal field is multidimensional and commonly transient with rock exhumation paths that have significant lateral and vertical components [e.g., *Stüwe et al.*, 1994; *Mancktelow and Grasemann*, 1997; *Ehlers et al.*, 2001; *Batt and Brandon*, 2002; *Ehlers et al.*, 2003]. The interpretation of thermochronometer data from such settings is more complex and benefits from the use of thermal models to generate realistic subsurface thermal fields. The model we use consists of three components: (1) a kinematic model (Figures 1c and 1d) that prescribes nodal advection velocities for (2) a thermal finite element model (Figure 3), which calculates temperature as a function of location and kinematic field, and (3) a thermochronometer age prediction model that generates sample ages at the surface as a function of their cooling rate. The following three sections detail the three model components. Table 1 lists the physical dimensions of the model and free parameters explored.

4.1. Kinematic Model

[13] In this study the fault kinematics of the Himalayan front are considered by partitioning slip between the MCT and MFT, assuming a constant convergence rate between India and Tibet of 20 mm/yr. We also take into account subduction of the Indian Shield and underplating of material from the Indian plate into the overriding wedge (Figures 1b–1d). Potential slip on the STF is not considered because the displacement history of the STF over the range of ages covered by the AFT data is unclear and poorly constrained in comparison with activity on the MFT or MCT [e.g., *Hodges*, 2000]. Furthermore, one model was run with the STF active at the same rate as the MCT and we saw no difference in the model predicted AFT ages within the sample uncertainties. We assume a shortening direction of 198° across thrust faults and that the Indian Shield moves north at 018°. The shortening direction is subparallel to the transport direction inferred from measured stretching lineations in the MCT shear zone [*Brunel*, 1986] and consistent with the present-day convergence direction between the Tibetan Plateau and India as measured by GPS [*Bilham et al.*, 1997; *Larson et al.*, 1999; *Wang et al.*, 2001; *Jouanne et al.*, 2004; *Zhang et al.*, 2004].

[14] Faults in the model are approximated as planar surfaces based on the geologic cross section of *Lavé and Avouac* [2000] (Figures 1b–1d) and tectonic map of *Searle and Godin* [2003] (Figure 2). The MFT splays off of the MHT and strikes perpendicular to the shortening direction at 288°. The MFT-MHT system dip angle varies with depth as shown in Figures 1c and 1d. The shallow southern section dips gently at 7°, the middle ramp section dips at 20° and the deep northern section dips at 8°, consistent with surface observations and microseismicity [*Lavé and Avouac*, 2000]. The strike of the MCT is a linear approx-
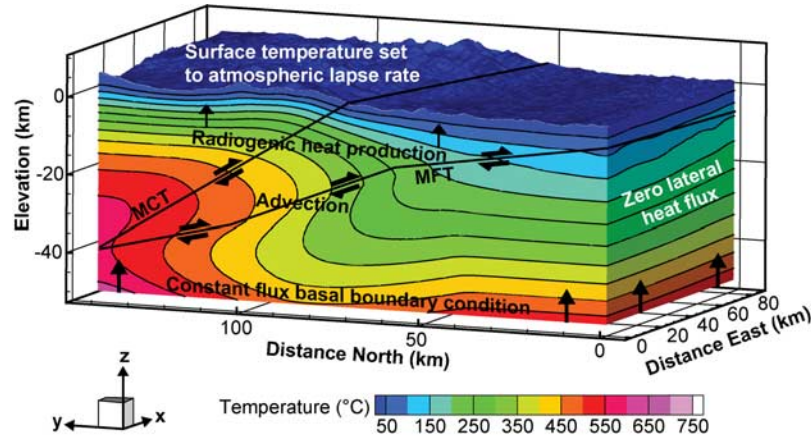
Figure 3. Three-dimensional block diagram of the thermokinematic model illustrating the boundary conditions and thermal model components. The kinematic model has the MFT and MCT active (thick lines). Abbreviations are as in Figure 1. Contoured temperatures (thin lines) show significant perturbation to the subsurface thermal field from the kinematic model and other thermal influences.

imation of the mapped MCT II trace of *Searle and Godin* [2003] (Figure 2) and it dips 28° NNE. The STF is not active in the kinematic models, but is included in the model geometry because it separates two model rock types with significantly different material properties: the GHS and TS. The STF is approximated as three linear segments with dip angles parallel to the MCT at 28° [*Macfarlane et al.*, 1992; *Hodges et al.*, 1996; *Searle and Godin*, 2003]. The structural geometry does not vary with time because most of our cooling ages are very young (<3 Ma). Although the structural geometry is likely to have changed over longer timescales, we suggest that this is the simplest scenario that still captures the plausible kinematic scenarios for Plio-Quaternary faulting. Comparison to the data later in the paper allows us to evaluate whether this degree of complexity is sufficient.

[15] Slip across faults is prescribed to honor the present-day geodetic convergence rate between India and Tibet of ~20 mm/yr [*Bilham et al.*, 1997; *Larson et al.*, 1999; *Wang et al.*, 2001; *Jouanne et al.*, 2004]. Convergence is partitioned between overthrusting on the MFT and MCT and underthrusting of the Indian Shield beneath the Himalaya. It is important to note that in our model, overthrusting and underthrusting refer to the horizontal component of motion, and should not be confused with the fault slip rate. The rate of underthrusting, $v_{underthrusting}$, is adjusted to honor the 20 mm/yr convergence rate depending on the overthrusting rate:

$$v_{underthrusting} = v_{obs} - (v_{MFT} + v_{MCT}) \qquad (1)$$

where v_{obs} is the Indo-Tibetan convergence rate and v_{MFT} and v_{MCT} are the overthrusting velocities of the MFT and MCT.

[16] The model uses the kink-band, fault-bend folding method of the thrust sheets [*Suppe*, 1983] and slip occurs parallel to the model fault planes. Mass is conserved in the model. The slip rate on an individual structure is a function

of the dip angle of the structure and the convergence rate across that structure. For each fault, the slip rate is calculated as

$$v_{slip,MFT} = (|v_{MFT}| + |v_{underthrusting}|) / \cos \theta_{i,MFT} \qquad (2a)$$

$$v_{slip,MCT} = |v_{MCT}| / \cos \theta_{MCT} \qquad (2b)$$

where $\theta_{i,MFT}$ is the dip angle of the ith dip plane of the MFT and θ_{MCT} is the dip angle of the MCT. Note that because the convergence rates are fixed in the model, the fault slip rate on different dip sections of the MFT will vary. Because of this, slip on individual structures will be referred to by the overthrusting rate across that structure. The ranges of overthrusting rates explored in the model are 1–15 mm/yr

Table 1. Numerical Model Parameters

Property/Parameter	Model Input Value
Material Properties	
GHS heat production	0.8–3.0 μW/m^3
LHS/Indian Shield heat production	0.8 μW/m^3
TS heat production	0.5 μW/m^3
Thermal conductivity	2.5–3.0 W/m K
Specific heat	800 J/kg K
Density	2750 kg/m^3
Numerical Parameters	
MFT overthrusting rate	1–15 mm/yr
MCT overthrusting rate	0–8 mm/yr
STF extension rate	0 mm/yr
Model time step	10^5 years
Horizontal node spacing	700 m
Average vertical node spacing	~1500 m
Surface temperature	14–7°C/km times elevation
Basal heat flow	20–50 mW/m^2
Model domain	84 × 140 × 58 km

across the MFT and 0–8 mm/yr across the MCT, as shown in Table 1.

[17] One objective of this study is to quantify the range of possible erosion rates over the last ~3 Myr, the time covered by the AFT data. Rock exhumation in this region of the Himalaya occurs by erosion, and because the model geometry and topography are static, the exhumation and erosion rates are dictated by the kinematic model. In this paper, we define the model exhumation rate to be the rate at which material approaches the model surface from depth parallel to the transport direction because the exhumation pathways have a significant component of lateral motion. This definition is slightly different than that used in many studies, where the exhumation rate is strictly related to vertical transport [e.g., *Ring et al.*, 1999]. In contrast, we define the model erosion rate to be the vertical component of the exhumation rate prescribed in the kinematic model. Thus the erosion rate at a given position (x, y, z) in the model, $v_z(x, y, z)$, is a function of the orientation of underlying structures and rate of overthrusting. The erosion rate $v_z(x, y, z)$ is

$$v_z(x,y,z) = v_{MFT} \tan \theta_{i,MFT} \qquad \{y_{MFT} < y < y_{MCT}\} \qquad (3a)$$

$$v_z(x,y,z) = v_{MFT} \tan \theta_{i,MFT} \ + \ v_{MCT} \tan \theta_{MCT} \qquad \{y > y_{MCT}\} \qquad (3b)$$

where y_{MFT} and y_{MCT} are the y coordinates of the MFT and MCT, at the x coordinate and z coordinate of the point of interest. The coordinate system has the x coordinate increasing to the east, y coordinate increasing to the north and z coordinate positive upward, as shown in Figure 3.

[18] Previous work has estimated long-term erosion rates in the Greater Himalayan zone to be several millimeters per year [e.g., *Burbank et al.*, 2003; *Thiede et al.*, 2004]. Using these results as a starting point, we chose combinations of fault kinematics that generate erosion rates between ~1–6 mm/yr in the Greater Himalayan zone. The kinematic simulations were divided into four subsets: (1) the MFT is the only active structure, (2) the MFT and MCT have equal overthrusting rates, (3) the MFT has a larger overthrusting rate than the MCT, and (4) the MCT has a larger overthrusting rate than the MFT. We did not simulate cases where the MCT was the only active structure because those models would not exhume samples south of the model MCT to the surface.

[19] We assume an incompressible material and conservation of mass. We also assume that the fault locations are fixed in the model, such that the MCT does not move with respect to the MFT when the MFT is active. Because of the steady state topography and the above assumptions, in kinematic scenarios b–d (e.g., Figure 1d), some of the subducting Indian Shield material is incorporated into the base of the LHS via underplating. This underplating balances the erosional removal of material south of the MCT.

4.2. Thermal Model

[20] The background thermal state of continental crust depends on heat flow into the base of the crust and material properties (e.g., thermal conductivity, radiogenic heat production). Deviations from this background state can occur in regions of active faulting, erosion, sedimentation, and/or with significant topographic relief [*Stüwe et al.*, 1994; *Mancktelow and Grasemann*, 1997; *Braun*, 2005; *Ehlers*, 2005]. Furthermore, in regions of rapid faulting such as the Himalaya, shear heating along faults can be significant [*Graham and England*, 1976; *Barton and England*, 1979; *Arita*, 1983; *England et al.*, 1992; *Henry et al.*, 1997]. We calculate the 3-D thermal field of a 140 × 84 × 50 km (L × W × D) region within the Himalayan front. Processes accounted for in the model include rock uplift due to faulting, erosion, topography, basal heat flow variations, and thermophysical material properties.

[21] The subsurface thermal field is calculated using the steady state advection-diffusion equation:

$$\frac{\nabla (K\nabla T)}{\rho c} - \bar{v}\nabla T = -\frac{A}{\rho c} \qquad (4)$$

where T is temperature and $\bar{v}$ is the material velocity. K, A, ρ and c are the thermal conductivity, radiogenic heat production per unit volume, density and heat capacity, respectively. The reasons for using the steady state advection-diffusion equation are discussed in section 4.3.2. Our modeling approach is similar to that of *Ehlers and Farley* [2003] and uses the finite element program FRACTure [*Kohl and Hopkirk*, 1995]. The thermal model is coupled to the kinematic model detailed in section 4.1 and used to solve Equation (4) in 3-D in an Eulerian (spatial) reference frame. By using a 3-D solution to equation (4), we are able to account for the effects of advection in three dimensions, short-wavelength (valley-ridge) and long-wavelength (Tibetan Plateau–Gangetic Plains) topography, and the effects of various material properties.

[22] We minimized the N-S spatial extent of the model, but kept it large enough to prevent the lateral boundary conditions from generating an unrealistic thermal influence because of the long-wavelength topography (Table 1). The upper surface of the model is derived from a 250-m digital elevation model of the region and has a constant temperature boundary condition. Upper surface temperatures were fixed at 14°C at sea level and decreased at an atmospheric lapse rate of 7°C per kilometer elevation increase. The basal boundary condition in the model is a constant flux, which is varied from 20 to 50 mW/m^2. These basal heat fluxes are in agreement with the values calculated from measurements of surface heat flow out of the Indian Shield [*Roy and Rao*, 2000]. Radiogenic heat production is set to 0.8 μW/m^3 for the Indian Shield and LHS which also yields surface heat flow values similar to the observations [*Roy and Rao*, 2000]. For the TS an average sedimentary rock heat production of 0.5 μW/m^3 is used [*Rybach*, 1976]. Heat production in the GHS is varied from 0.8 to 3.0 μW/m^3, similar to the range represented by previous measurements [*England et al.*, 1992]. Thermal conductivity measurements from rocks sampled in the study area average 3.35 ± 0.85 W/m K at room temperature (Table A1). Thermal conductivity for the model domain is fixed at either 2.5 or

3.0 W/m K, similar to the temperature-corrected measured values [*Sass et al.*, 1992; *Clauser and Huenges*, 1995]. The ranges of material properties investigated are summarized in Table 1.

4.3. Model Assumptions

[23] We make several simplifying assumptions in an effort to capture the important thermal influences, but not overcomplicate the model.

4.3.1. Assumption 1: Topographic Steady State

[24] The assumption of topographic steady state was used here for several reasons. First, at this point we have no clear way of constraining how topography has changed over the last >3 Ma. The additional free parameters required to simulate evolving topography would not be well constrained and we have chosen instead to work with the smallest set of assumptions possible in the modeling. Second, several lines of evidence suggest that major changes in the position of fluvial systems have not occurred recently. If relief changes occurred, they may have happened over relatively short timescales (<10 kyr) [*Gabet et al.*, 2004], and the magnitude of relief change is likely smaller than the average AFT sample age uncertainties. Although little evidence of the paleoriver locations exists, the south flowing rivers draining the southern margin of the Tibetan Plateau are suggested to have flowed along similar paths for several million years [e.g., *Gupta*, 1997]. Work in progress is testing our assumption of topographic steady state over the time period samples cooled. More specifically, we are evaluating what data and modeling approaches are required to quantify changes in relief and drainage locations in the Marsyandi valley (e.g., approach of *van der Beek et al.* [2002] and *Braun and van der Beek* [2004]).

[25] *Stüwe et al.* [1994] showed from a 2-D thermal model that, at increasingly high erosion rates, the AFT closure isotherm will move to shallower levels in the crust and more closely mimic the overlying topography. Assuming a horizontal AFT closure isotherm beneath 5 km high topography, the difference in distance from the isotherm to surface under peaks versus valleys is 5 km. At an erosion rate of 5 mm/yr, the depth to the isotherm becomes shallower and the difference in isothermal depth between peaks and valleys decreases to ~1 km [*Stüwe et al.*, 1994]. Although the shorter-wavelength relief between valleys and ridges in our study area may have changed over the time interval to which our samples are sensitive (average AFT cooling age of 1.0 Ma), we have no reason to doubt that the major topographic influences were likely in place for the time during which most samples cooled.

[26] *Braun* [2002] showed that longer-wavelength topography will cause the subsurface isotherms to be disturbed to greater depths than shorter-wavelength topography. Thus lower-temperature thermochronometers will be more sensitive to shorter-wavelength topography than higher-temperature systems. For example, the largest topographic influences on subsurface thermal gradients are the long-wavelength, north-south elevation changes across the Himalayan front and shorter-wavelength, east-west oriented

topography across the Marsyandi drainage. Predicted $^{40}Ar/^{39}Ar$ cooling ages are more likely sensitive to the long-wavelength topography [*Brewer et al.*, 2003], whereas the shorter-wavelength, valley-ridge topography is likely to influence the AFT ages. The first-order, valley-ridge topographic features are at least as old as most of the AFT cooling ages (~1.0 Ma) and the Tibetan Plateau, the major north-south topographic influence, is thought to have been at high elevation since at least the late Miocene [*Harrison et al.*, 1992; *Tapponnier et al.*, 2001]. Second-order variations in the topography through time, such as several hundred meters of changing relief across the Marsyandi drainage or variations in shorter-wavelength topography, are possible in this area, but are not constrainable with the data due to large uncertainties in sample ages. For additional discussion of how the wavelength of topography can influence thermochronometer ages, see *Braun* [2002].

[27] AFT sample locations where steady state topography is clearly unrealistic have been excluded from our analysis (Bagarchhap, Chame, Dharapani transects; A–C in Figure 2). For these transects, the sampled ridges are oriented such that they have steeper slopes than the fault transporting those samples to the surface in the model. When particles coincident with the sample locations are tracked back in time to generate thermal histories, those samples exit the model domain, travel through the air above the model surface and later reenter the model. This generates unrealistic predicted cooling ages. We instead focus on samples that have had the simplest exhumation history, where particle tracking generates simple thermal histories (Khudi, Jagat, Nagi Lek, Syange, Tal transects; D–J in Figure 2). Although significant topographic change has likely occurred in this area, we have minimized its effect on our interpretation by focusing on the vertical transects sensitive to the dominant topographic features in the region. The remaining transect locations (Bagarchhap, Chame, Dharapani transects; A–C in Figure 2) are the focus of work in progress interpreting the topographic evolution of subsidiary drainages in the region.

4.3.2. Assumption 2: Thermal Steady State

[28] *Stüwe et al.* [1994] showed that a transient thermal field will approach steady state more quickly at higher erosion rates. For example, at erosion rates of 1 to 5 mm/yr, thermal equilibration within 20% of steady state is achieved in 20 to 4 Myr, respectively. If the Himalayan front has been present and eroding since at least the late Miocene [*Harrison et al.*, 1992; *Tapponnier et al.*, 2001], then subsurface thermal field has likely approximated a steady state within the uncertainties in the data.

4.3.3. Assumption 3: Significant Shear Heating

[29] Shear heating is included to account for frictional heating on the fault planes using the methods of *Henry et al.* [1997]. We follow the moderate friction case of *Hansen and Carter* [1982], where the fault zone is assumed to be 1 km wide and the strain rate is equal to the slip rate across the fault. The maximum allowed shear stress is 50 MPa and calculated as the minimum of either a brittle, pressure-dependent law or ductile, temperature-dependent power law. The additional heat produced is added to the nodal

radiogenic heat production within the shear zone. The slip rates on the faults are fairly high (e.g., Table 1) and produce significant shear heating.

4.3.4. Assumption 4: Negligible Heat Transfer by Fluid Flow

[30] Recent work by *Evans et al.* [2004] suggests advective heat transfer by fluids may be significant in the Greater Himalayan zone. Although the effect of heat transfer by fluids may be important, its significance relative to rapid advective heat transfer by rock exhumation is unknown [e.g., *Ehlers*, 2005]. For this study we make the same assumption as all other thermochronometer studies to date and assume conductive heat transfer and advective heat transfer by rock exhumation are the dominant thermal processes. Simulating heat transfer by fluid flow is beyond the scope of this study, largely due to the additional unconstrained parameters in the model. Additional work in progress by the authors is evaluating the influence of fluid flow on thermochronometer ages.

4.4. Thermochronometer Age Prediction

[31] Thermochronometer ages are calculated using model-derived cooling histories for particles coincident with the sample locations. Cooling histories were generated by tracking samples from the surface back to different depths in the steady state thermal model for the last 20 Myr. Note however that only the last ~3 Myr of the cooling history is important because most of the AFT samples cooled at this time. Predicted AFT ages were calculated using the *Laslett et al.* [1987] kinetic annealing algorithm as implemented by *Ehlers et al.* [2003]. Muscovite $^{40}Ar/^{39}Ar$ ages are also predicted from the sample cooling histories, but the kinetics of argon diffusion in muscovite are not understood in detail. Because of this, we report the predicted ages as the time since the rock cooled below 350°C, but we regard this as a minimum estimate for the closure temperature and use it only for illustrative purposes of how a higher-temperature thermochronometer responds to different kinematic scenarios.

5. Results

[32] In our modeling approach, we evaluated discrete combinations of model parameters from the range of plausible values (Table 1). This approach evaluates the parameter space and identifies the range of geologically possible scenarios (e.g., slip partitioning, material properties, basal heat flux) that produce the observed cooling ages. In total, this required 397 simulations. In the following sections, we discuss the influence of each of these parameters and test the sensitivity of the predicted ages to these variables. The parameter of interest in each section is varied across the chosen range of values, while all the other free parameters are fixed at average values. Ages predicted from the Nagi Lek transect sample locations (transect J in Figure 2) are shown because this transect is oriented such that the predicted ages are least likely to be affected by the steady state topography, and the transect has a large elevation range and number of samples. The dominant effects on cooling ages discussed below are similar for the other transects. We

plot model predicted ages using nominal AFT and $^{40}Ar/^{39}Ar$ uncertainties of 20% and 10% of the sample age, respectively, to highlight which processes are significant within typical sample uncertainties.

[33] It is important to note that in regions with potentially high exhumation rates, such as the Greater Himalayan zone, the thermal field of the upper crust may be dominated by erosion and advective heat transfer [e.g., *Ehlers*, 2005]. The implication of having a highly advection-dominated thermal field is that thermal gradients might be less sensitive to other thermal processes and parameters (e.g., basal heat flow, material properties, etc). To the best of our knowledge, no study has systematically evaluated which processes and parameters are important for the interpretation of thermochronometer ages in rapidly eroding regions. Furthermore, in the discussion below for each parameter, the change in cooling ages due to variations in the explored parameter will likely only apply to rapidly eroding regions. In other words, the same magnitude change of a given parameter in a region that is eroding more slowly will likely have a larger effect than shown here. In the next several sections we evaluate the relative significance of each parameter in the model for a moderately rapid erosion rate of the Greater Himalayan zone of 2.5 mm/yr.

5.1. Effect of Basal Heat Flux on Predicted Ages

[34] Increasing the heat flux into the base of the thermal model increases the maximum temperature within the model domain and steepens the thermal gradient near the surface. As a result, the distance traveled from a given closure isotherm to the surface decreases. Thus ages predicted from models with higher basal heat flux are younger than those from models with lower basal heat flux (Figure 4). We model varying basal heat fluxes of 20, 35 and 50 mW/m^2, while thermal conductivity is set to 2.5 W/m K, heat production in the GHS is specified as 1.9 μW/m^3, and shear heating is included. The kinematic model has 4 mm/yr of overthrusting for the MFT and 2 mm/yr for the MCT.

[35] A 2.5-fold increase in the basal heat flux leads to predicted AFT ages that are younger by ~10%, whereas the muscovite $^{40}Ar/^{39}Ar$ ages become ~15–20% younger (Figure 4). When the uncertainties are considered for both sets of predicted ages, they are statistically indistinguishable for all three heat flux values, although if age uncertainties were <10% for the predicted $^{40}Ar/^{39}Ar$ ages, the effect of a threefold change in basal heat flux would be statistically discernable. Because the AFT data lack sensitivity to the basal heat flux, they cannot be used to constrain the range of tested values. Considering the measured surface heat flux data in India, the most likely basal heat flux values are 20–35 mW/m^2 [*Roy and Rao*, 2000]. In addition, although the influence of basal heat flux variations is not significant in this study, we note that at slower erosion rates typical of other mountain ranges the influence of basal heat flow on near-surface thermal gradients can be significantly larger.

5.2. Effect of Heat Production on Predicted Ages

[36] Increasing the radiogenic heat production in the GHS is predicted to have a major impact on exhumed thermo-
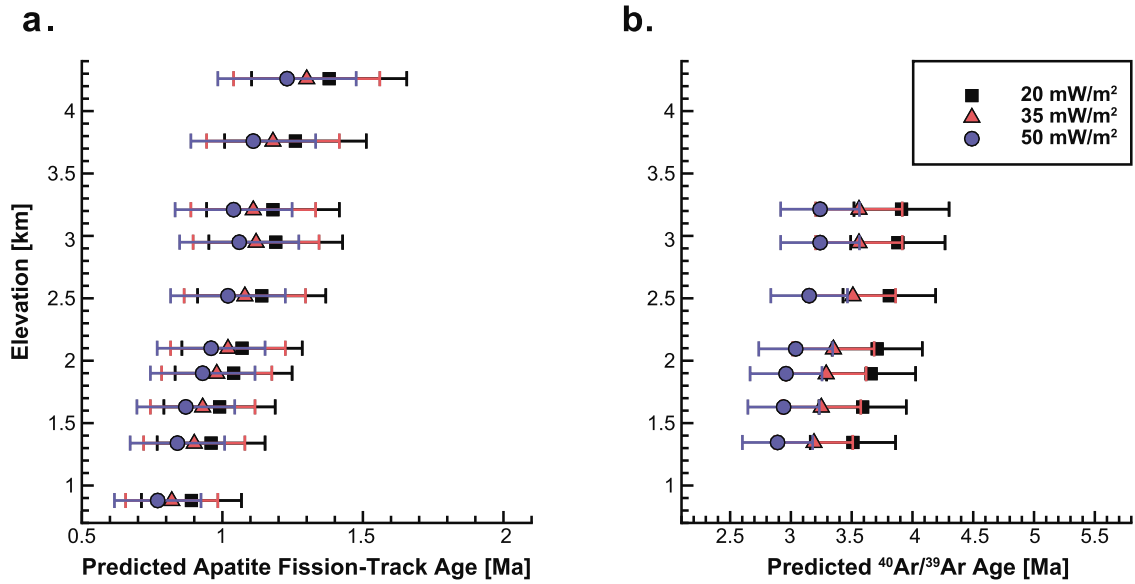
a.

b.

Figure 4. Effect of varying basal heat flux on predicted sample ages for the Nagi Lek transect. Predicted (a) apatite fission track (AFT) and (b) muscovite ^{40}Ar/^{39}Ar ages versus sample elevation for models with basal heat flux values of 20, 35, and 50 mW/m^2 (squares, triangles, and circles). Age error bars are 20% and 10% for the AFT and ^{40}Ar/^{39}Ar, respectively.

chronometer sample ages (Figure 5). The three models shown here have heat production values of 0.8, 1.9 and 3.0 μW/m^3, basal heat flux of 35 mW/m^2, thermal conductivity of 2.5 W/m K, and include shear heating. The

kinematic model has a rate of overthrusting of 4 mm/yr for the MFT and 2 mm/yr for the MCT.

[37] Similar to the case for varying basal heat flux, higher heat production values steepen the thermal gradient near the model surface, leading to younger predicted ages. For an
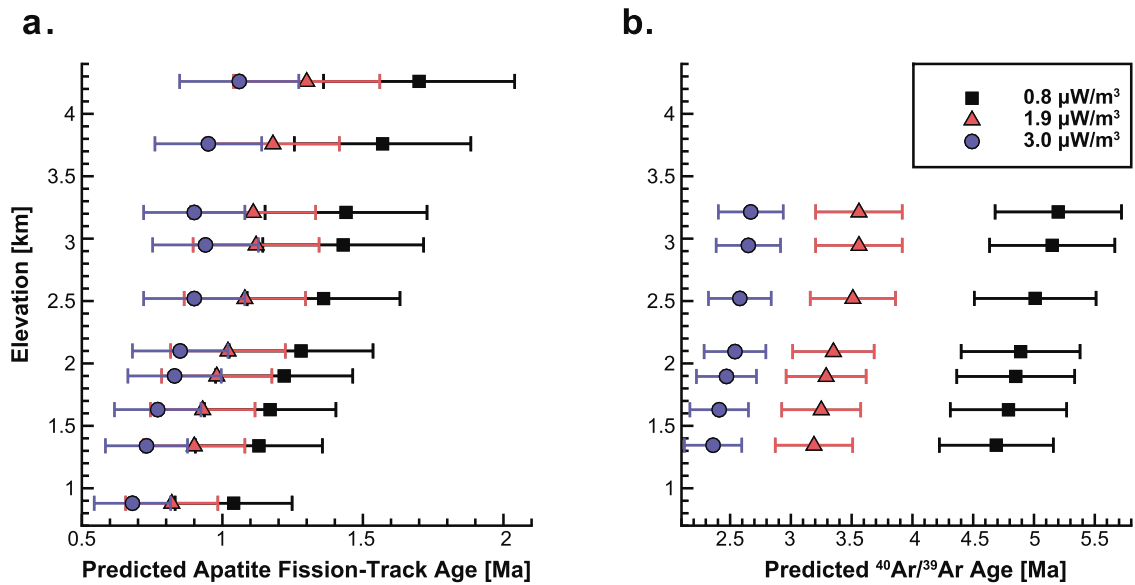
a.

b.

Figure 5. Effect of varying Greater Himalayan sequence heat production on predicted sample ages. Predicted (a) apatite fission track (AFT) and (b) muscovite ^{40}Ar/^{39}Ar sample ages versus sample elevation for models with heat production values of 0.8, 1.9 and 3.0 μW/m^3 (squares, triangles, circles). Age error bars are 20% and 10% for the AFT and ^{40}Ar/^{39}Ar, respectively.
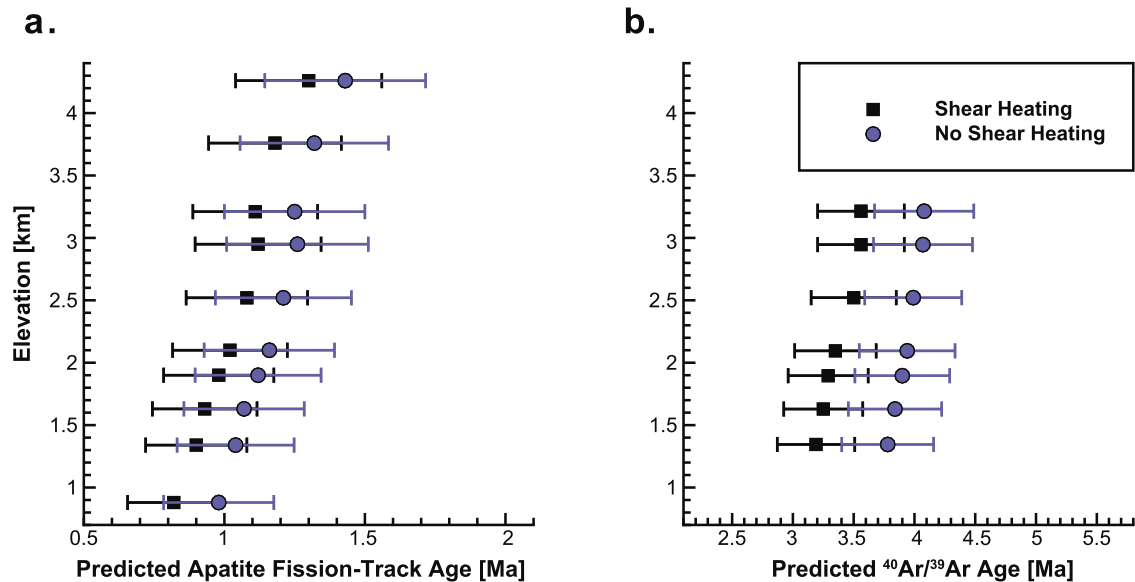
Figure 6. Effect of shear heating on predicted sample ages. Predicted (a) apatite fission track (AFT) and (b) muscovite [40]Ar/[39]Ar sample ages versus sample elevation for models with and without shear heating (squares, circles). Age error bars are 20% and 10% for the AFT and [40]Ar/[39]Ar, respectively.

increase in heat production from 0.8 to 1.9 $\mu W/m^3$, the AFT and muscovite [40]Ar/[39]Ar ages are ~0.2–0.4 Myr and ~1.5–1.7 Myr younger, respectively, with a greater difference in age at higher elevations (Figure 5). Despite the large assigned uncertainties on the AFT ages, ages from the highest heat production model are statistically distinguishable from those generated from models with lower heat production: a fourfold increase in heat production causes a >35% decrease in predicted age. The [40]Ar/[39]Ar ages, show an even larger sensitivity to different heat production values. However, because the AFT data are only modestly sensitive to heat production variations, we are unable to eliminate any of the range of tested values using the model (Table 1). Muscovite [40]Ar/[39]Ar data should be able to constrain the range of tested values. Measurements of heat-producing element concentrations yield an average volumetric heat production value of 2.1 $\mu W/m^3$ (Table A2). Thus our preferred heat production values are 1.9 and 3.0 $\mu W/m^3$, due to the high concentration of heat-producing elements in the GHS [*England et al.*, 1992].

5.3. Effect of Shear Heating on Predicted Ages

[38] The magnitude of heat contributed to the thermal field from shear heating depends on the fault slip rate, temperature and pressure at a location within the shear zone [*Henry et al.*, 1997; *Bollinger et al.*, 2006]. We assess two models: one that includes shear heating; the other not (Figure 6). Both models have basal heat flux values of 35 mW/m^2, heat production of 1.9 $\mu W/m^3$ and thermal conductivity of 2.5 W/m K. The prescribed kinematics are 4 mm/yr of overthrusting for the MFT and 2 mm/yr for the MCT.

[39] With the given kinematic field, predicted AFT ages are ~0.2 Myr younger and predicted [40]Ar/[39]Ar ages are

~0.8 Myr younger with the addition of shear heating. Despite this ~15% decrease in predicted ages, neither the AFT ages nor the [40]Ar/[39]Ar ages are statistically different within error bars. Because our AFT data show insufficient sensitivity to shear heating, we are unable to rule out shear heating. However, the difference in lower crustal temperatures between models with and without shear heating is significant (~50–100°C). Thus we include shear heating in the model simulations in the event that it becomes more significant when predicting [40]Ar/[39]Ar ages at slower exhumation rates, when advective heat transfer processes are less dominant in the thermal field.

5.4. Effect of Thermal Conductivity on Predicted Ages

[40] Increasing the thermal conductivity in the thermal model decreases the maximum temperature and causes the thermal gradient to be less steep (Figure 7). This decrease in temperature leads to comparatively older predicted ages. In the example shown, the thermal conductivity is varied between 2.5 and 3.0 W/m K and the kinematic field has overthrusting of 4 mm/yr for the MFT and 2 mm/yr for the MCT. The models each have basal heat flux values of 35 mW/m^2, heat production of 1.9 $\mu W/m^3$ and include shear heating.

[41] AFT and [40]Ar/[39]Ar ages predicted from the thermal model with a thermal conductivity of 3.0 W/m K average ~0.2–0.3 and ~0.9–1.0 Myr older, respectively, than those from the model with lower thermal conductivity. With the error bars, the AFT ages for both scenarios cannot be distinguished, but muscovite [40]Ar/[39]Ar data should be sensitive to thermal conductivity variations. Because the AFT data are likely not sufficiently sensitive to variations in thermal conductivity, we cannot exclude any of the values used in this sensitivity test. Measurements of the thermal
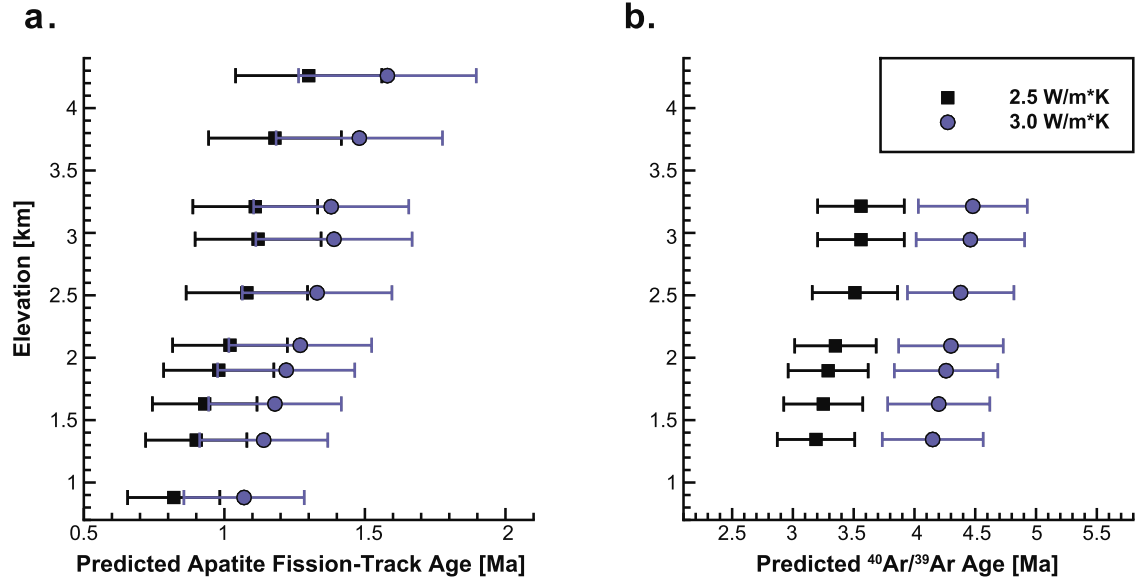
a.

b.

Figure 7. Effect of varying thermal conductivity on predicted sample ages. Predicted (a) apatite fission track (AFT) and (b) muscovite ^{40}Ar/^{39}Ar sample ages versus sample elevation for models with thermal conductivity values of 2.5 and 3.0 W/m K (squares, circles). Age error bars are 20% and 10% for the AFT and ^{40}Ar/^{39}Ar, respectively.

conductivity in rocks from the GHS show a temperature-corrected average value of 2.75 W/m K that is intermediate to the tested values of 2.5 and 3.0 W/m K (Table A1).

5.5. Effect of Fault Kinematics on Predicted Ages

[42] The kinematic field that drives advection in the thermal model has a strong influence on predicted samples ages. In the previous sections, the effects of different model parameters were shown by the variations in predicted ages within a given parameter space. In this section, we test 22 different kinematic fields and find the kinematic influence tends to dominate the variations in other model parameters. Because of this, the data are plotted in a manner that shows which kinematic models best fit the observed ages. However, rather than show the overthrusting rates for each fault, the plots list the different kinematic models by their erosion rate (v_z, Equation (3)) in subplots for the different tectonic scenarios (Figure 8). The listed erosion rates are for the Greater Himalayan zone in the model, the region where most of the samples were collected. Thus, for a given kinematic model, nearly all of the samples should be vertically exhumed at the same rate. The other velocity components (v_x and v_y) can be calculated using Equation (3) and the structural geometry, as discussed in section 4.1. The quality of fit of the predicted ages to the observed is quantified using the square root of a modified, reduced chi-square misfit,

$$\chi^2 = \sqrt{\frac{\sum_{i=1}^{N}\left(\frac{\text{Age}_{p_i} - \text{Age}_{o_i}}{U_i}\right)^2}{N}} \qquad (5)$$

where Age$_{pi}$ is the ith predicted age, Age$_{oi}$ is the ith observed age, U_i is the one sigma uncertainty in the ith age, and N is the number of samples in the summation. χ^2 values are always greater than or equal to zero, with zero representing a perfect fit to the data and increasing values representing greater misfit.

[43] Because erosion rates are linked directly to predicted cooling ages and are dictated by fault slip rates in the context of a fixed topographic surface, minimizing the misfit between predicted and observed cooling ages yields the erosion rates that best fit the data (Figure 8). The χ^2 misfit values were calculated for ages predicted from the Nagi Lek transect (J in Figure 2) for each of the kinematic models shown. The GHS heat production was fixed at 3.0 μW/m^3, shear heating was included and the thermal conductivity was 2.5 W/m K. The χ^2 minima in the subplots (Figure 8) show the kinematic fields that provide the best fit to the data (shaded region). The data are best fit by χ^2 values that are ≤ 2, which generally represent models where the predicted ages are within the 2σ uncertainties of the data. In all of the plots, the initial decrease in misfit to a minima and subsequent increase at higher erosion rates reflects predicted ages that are too old at slow rates and too young at higher rates. The χ^2 misfit values for the AFT data in the Nagi Lek transect show they are best fit with average erosion rates between ~2.0 and 4.5 mm/yr. Thus these data are sensitive to the erosion rate, but not to the partitioning of slip on to different thrusts. This result is discussed in more detail in section 6.2.

6. Discussion

[44] The previous results demonstrate the sensitivity of predicted AFT and muscovite ^{40}Ar/^{39}Ar ages to different
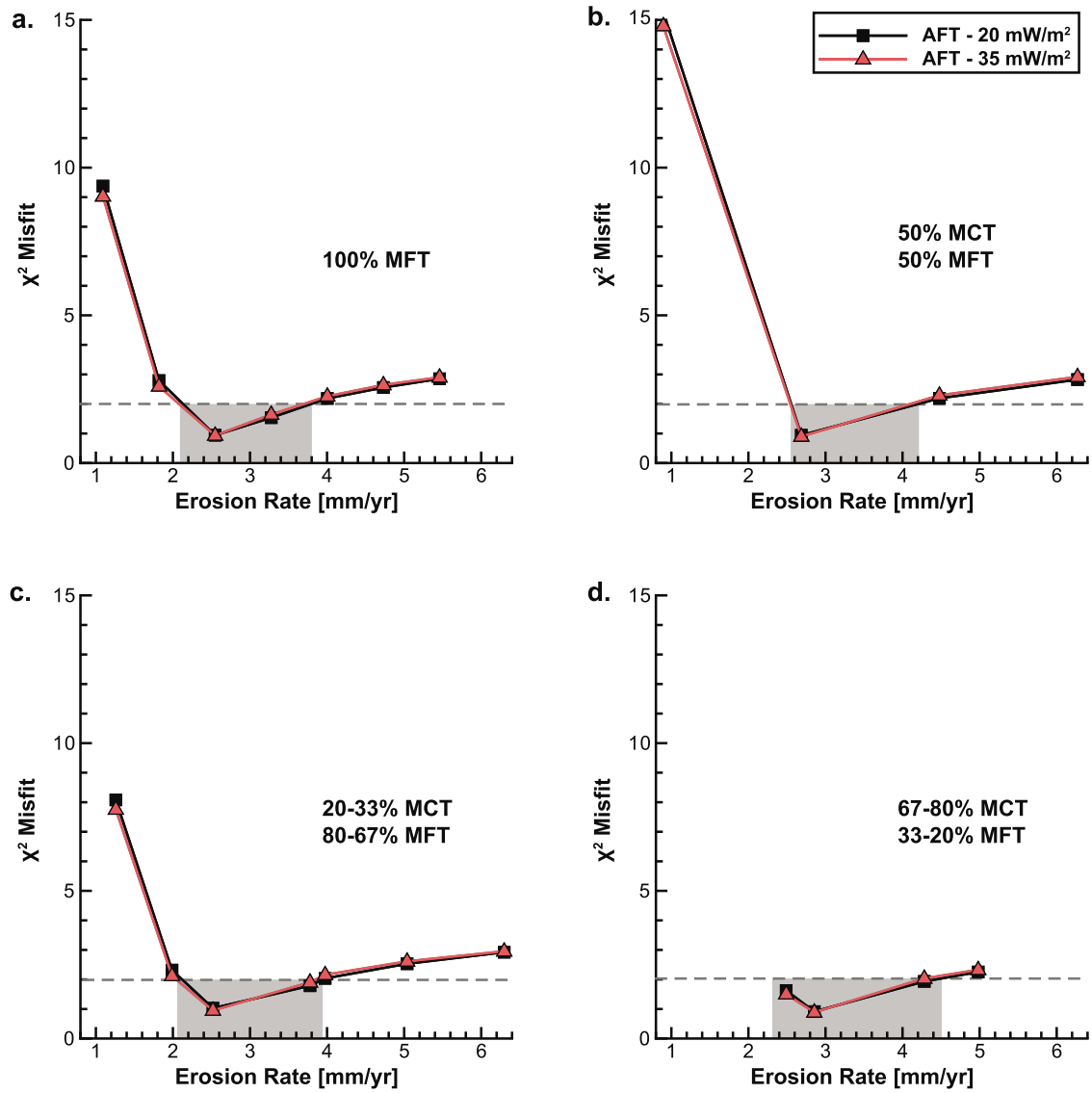
Figure 8. Effect of varying fault kinematics on predicted sample ages. The χ^2 misfit values for predicted and observed AFT ages versus erosion rates derived from various thermokinematic models with basal heat flux values of 20 and 35 mW/m^2 (squares, circles). Four different tectonic scenarios are shown: (a) slip only on the MFT, (b) equal overthrusting rate on the MFT and MCT, (c) larger overthrusting rate on the MFT than the MCT, and (d) larger overthrusting rate on the MCT than the MFT. The range of model-derived erosion rates that provide a good fit to the AFT data (shaded region) is constrained by χ^2 misfit values of ≤ 2 (dashed line). Abbreviations are as in Figures 1 and 2.

thermophysical processes and material properties in the crust. The dominant message conveyed by these results is an acute sensitivity of predicted ages to the erosion rate generated by different kinematic fields. Simply put, in a rapidly eroding region such as the Himalayan front, the thermal field is dominated by advective heat transfer from rock exhumation. Whereas for the other processes and material properties considered (e.g., basal heat flow, heat production, conductivity, etc.) a twofold to threefold increase causes a noticeable change in exhumed sample ages, the difference in predicted ages is generally within sample age uncertainties. In contrast, a similar change in erosion rates produces a readily documentable variation in predicted ages.

[45] It should be noted that the insensitivity of sample AFT ages to most thermal model parameters (Figures 4–7) will not apply to other active orogens if the exhumation rates are slower (<~1 mm/yr) and the thermal field more conductive than the simulations shown here. Moreover, much of this insensitivity emerges from the relatively large uncertainties assigned to the AFT ages (20%). For thermochronometer samples with smaller uncertainties, the sensi-

tivity to all parameters would increase. In the following sections, we revisit the influence of the kinematic field on thermochronometer ages and evaluate the erosion and kinematic history of the Greater Himalayan zone.

[46] Despite the previously highlighted dominance of advective heat transfer on the Greater Himalayan zone, it is important to note that nonuniqueness exists in the model results and trade-offs between different model parameters can produce nearly identical thermochronometer ages. The ages predicted from the thermokinematic model depend on the basal heat flux into the model, radiogenic heat production and thermal conductivity within the model, and the prescribed kinematic field and resultant shear heating. With five free parameters in the models, several combinations of variables provide an equal quality of fit to the thermochronometer data. This is not surprising, given the possible trade-offs in thermal influences between, for example, increasing heat production while decreasing basal heat flux. Our goal in evaluating which variables provide the best fit to the data is to constrain the range of free parameters and create a preferred parameter space.

[47] Another important point is that the erosion rates calculated from the models are average erosion rates and may mask shorter-timescale variations in exhumation. For instance, ages generated by slow exhumation followed by a pulse of rapid exhumation may be fit by a model that has an intermediate exhumation rate. One sign of such a misfit is when model-predicted ages match the average age of the observed ages, but do not follow the age-elevation trend of those data. Models that include transient variations in the thermal field would be required to fit such a trend and are beyond the scope of this paper.

6.1. Fit of Predicted Ages to Data

[48] In general, the predicted AFT ages from the best fit models fall within the 2σ uncertainties of the data for a given transect, yet predicted ages for some transects do not. We compare observed ages and their apparent erosion rates with predicted ages and the model-derived erosion rates for most transects (Figure 9). The Bagarchhap, Chame and Dharapani transects (A–C in Figure 2) are not shown because the assumption of steady state topography in the model is clearly violated when predicting cooling ages for samples collected on hillslopes that are parallel to or steeper than the rock exhumation trajectory prescribed by the kinematic model, as discussed in section 4.3.1.

[49] The predicted ages shown for each transect are from the best fit kinematic models for each tectonic scenario, with a basal heat flow of 20 mW/m^2, GHS heat production of 3.0 μW/m^3 and thermal conductivity of 2.5 W/m K. With the exception of the two Khudi transects, nearly all of the ages predicted from the best fit kinematic models are within the 2σ uncertainties of the data. This suggests that the model realistically simulates the major thermal and kinematic influences. This also implies that there have been no major changes in the topographic relief since the samples cooled, because the model topography is in a strict steady state and the model yields predicted ages that fit the data. It is worth noting, though, that much of the data

have large uncertainties, which may mask signs of relief change or other factors affecting the cooling ages.

[50] The predicted ages do not fit the data well for the two Khudi transects (Figures 9b and 9c). For the Khudi East transect (F in Figure 2), the misfit reflects the limited number of kinematic models that were run. Best fit predicted ages from kinematic scenarios b and d (erosion rates of 2.7 and 2.5 mm/yr) are generally too young to fit the data. For those scenarios, a kinematic model that generates a slightly slower erosion rate ($\sim$2 mm/yr) would likely provide a better fit. For the Khudi West transect (E in Figure 2), it appears that the data cannot be fit simply by using models with different erosion rates. For the models with slip on the MCT, the predicted ages are too old at low elevations and too young at high elevations. This is because the lowest two samples in the Khudi West transect are in the footwall of the MCT in the model, rather than the hanging wall (Figure 2). The lowest two samples are not likely to be strongly affected by slip on the MCT in the model and require fairly high overthrusting rates on the MFT to generate predicted ages that fit the observations. Because the MCT is riding atop the material moved along the MFT, any additional slip on the MCT leads to predicted ages in the model hanging wall that are too young to fit the data.

[51] Notably, the data-derived apparent exhumation rates can differ significantly from the model erosion rates (Figure 9). For a majority of transects, the apparent exhumation rate is greater than the model-derived erosion rate. Commonly, a nearly 50% difference separates these two rates. At least two factors affect the data-derived rates. First, because the regressions are error-weighted, a single age with a small error near the top or base of a transect can exert a strong influence on the regression line slope. Hence a young age high in the section can produce a negative slope. Second, overestimated erosion rates likely reflect a violation of one or more of the assumptions required to interpret regression line slopes as erosion rates on age-elevation plots of thermochronometer data, i.e., the samples must follow vertical exhumation paths and either be collected in a strictly vertical profile or the closure isotherm geometry must not be perturbed by the overlying topography. Low-temperature thermochronometer isotherms are likely to be perturbed by the overlying topography because of their shallow crustal depth. An exception to previous discussion is evident for the Syange transects (Figures 9d and 9e), where the apparent erosion rate is lower than the model-predicted rate. On these transects the slope of the regression line through the data is less than the trend in the predicted ages. One possible explanation for this trend is an acceleration in postclosure erosion. If the AFT samples pass through their closure isotherm at a slow rate and are subsequently brought to the surface at a slightly higher rate, the ages would be young, but the slope of the ages on an age-elevation plot would be shallow. The trend could also be explained by the effects of changing relief or groundwater flow, which are discussed in detail in section 6.3. Work in progress is exploring these ideas.

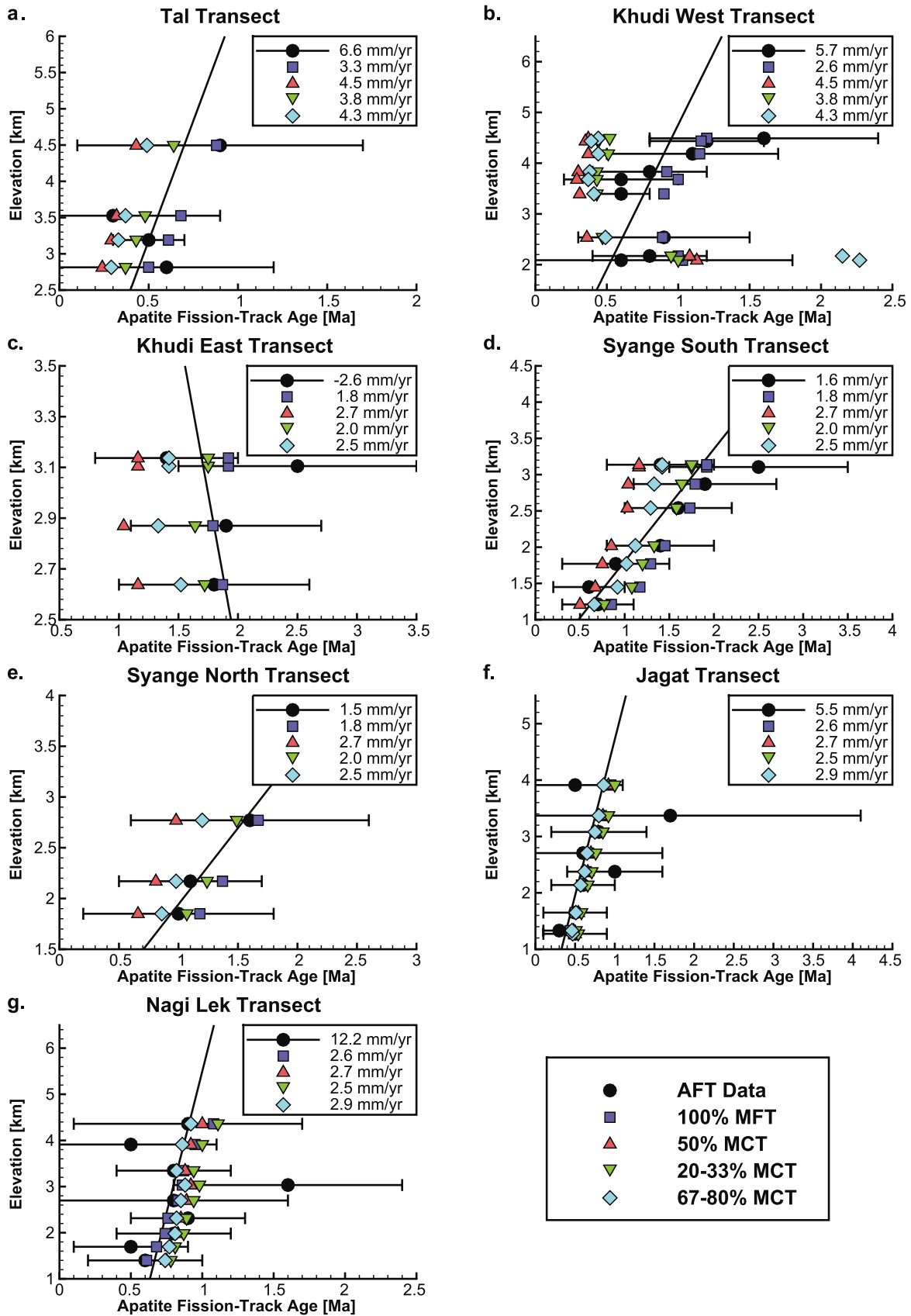[52] In addition to predicting AFT ages for the data transects, we predicted muscovite ^{40}Ar/^{39}Ar ages to com-

Figure 9

pare to ages from elsewhere in the Himalaya (Figure 10). The $^{40}Ar/^{39}Ar$ ages were predicted for the same transects and using the same models as the AFT predicted ages shown in Figure 9. The predicted $^{40}Ar/^{39}Ar$ ages are very young, no older than 5.5 Ma, with an average age of ~3.5 Ma. These ages are generally younger than those seen at similar structural positions within the Himalaya. Detrital muscovite $^{40}Ar/^{39}Ar$ ages in the GHS from two studies in the Marsyandi drainage have average ages of ~5 and ~7 Ma [*Ruhl and Hodges*, 2005; *Brewer et al.*, 2006]. This suggests that our $^{40}Ar/^{39}Ar$ ages were predicted using a model with an erosion rate that was too fast, leading to predicted ages that are too young. Because we are able to fit the AFT data with those erosion rates, however, this implies that erosion rates were slower prior to the time covered by the AFT data. The cause of the acceleration in erosion could either reflect a change in the tectonic forcing or regional/global climate. As noted by *Huntington et al.* [2006] and *Huntington and Hodges* [2006], little evidence exists to support a large-scale tectonic change, so climate is the more likely driver of accelerated exhumation. Timing of this inferred acceleration in erosion coincides with an intensification of northern hemisphere glaciation [*Raymo*, 1994], establishment of the modern-day summer and winter monsoon system [*Gupta and Thomas*, 2003] and a global increase in sedimentation rates and grain sizes [*Zhang et al.*, 2001]. More bedrock muscovite $^{40}Ar/^{39}Ar$ data from the model region would be necessary to quantify this apparent acceleration.

6.2. Is Out-Of-Sequence Faulting Significant?

[53] One of the uncertainties in the evolution of the Himalaya in central Nepal is whether or not there has there been large-magnitude out-of-sequence displacement near the trace of the MCT system subsequent to early Miocene time. The AFT cooling ages range from ~0 to 4 Ma, allowing us to investigate the history of activity on the MCT using kinematic models with and without slip on the MCT during this time period.

[54] We have explored various kinematic models in terms of quality of fit to the AFT data (Figure 8). If the AFT data are sensitive to the different tectonic scenarios, we should expect to see a better fit for one of those scenarios, as expressed by the χ^2 misfit values. What we observe in the AFT data, however, is that an equal fit ($\chi^2 < 2$) to the data can be attained by kinematic models with or without activity on the MCT. Furthermore, the fit of the predicted ages to the observed ages (Figure 9) shows that the predicted ages depend more on the erosion rate generated by the kinematic models than the kinematic scenario. In Figures 9f and 9g this is particularly clear, with the predicted ages plotting nearly atop each other for the different kinematic scenarios with similar erosion rates.

[55] The similar χ^2 misfit values for the AFT data in the best fit simulations are likely the result of models that produce similar thermal fields. At high vertical exhumation rates, the closure isotherm for the AFT system is advected to within several kilometers of the model surface and the near-surface (<5 km) thermal field differs less between different kinematic scenarios. In addition, the trajectories of particles transported along the MCT or MFT are different by only 8° in our model. We infer that the similarities in near-surface thermal fields and rock exhumation trajectories generate χ^2 misfit values for the AFT data in the best fit models that are comparable for all of the tectonic scenarios. In rapidly eroding regions, higher-temperature chronometers (e.g., muscovite or hornblende $^{40}Ar/^{39}Ar$) may be more sensitive to the fault kinematics because their age will be a function of a longer thermal history. In other words, higher-temperature data will integrate information over a greater distance and potentially be more sensitive to slight differences in rock exhumation trajectory. The model-predicted $^{40}Ar/^{39}Ar$ ages (Figure 10) support this idea, and several transects show sensitivity to the different kinematic scenarios. Slower erosion rates would increase the sensitivity to the kinematics, with ages that are statistically different including the assigned 10% error bars for several transects. On the other hand, using thermochronometers representing higher-temperature data puts more demands on the model assumptions. The assumed kinematic and topographic geometries have to remain constant through longer intervals of time; assumptions that become less likely with increasing age.

6.3. Spatial Variations in Erosion

[56] In the kinematic model, most of the sample locations are within the same thrust sheet and above planar faults dipping at constant angles, so the majority of samples are exhumed at the same rate for a given tectonic scenario. Despite spatially uniform exhumation histories, predicted sample ages at similar elevations vary across the model domain because of the thermal influences of the overlying topography, proximity to the faults and material properties. If the model geometry, material properties and assumption of steady state topography are realistic, at least one kinematic model should provide a good fit to all of the AFT data.

[57] Within the range of erosion rates that produces predicted ages that fit at least 80% of the observed ages on individual transects, none of our models can fit the data for all transects. Across our data set, erosion rates vary by about twofold (Figure 11), as calculated from the data

Figure 9. Fit of AFT predicted ages to observed ages in transects for different kinematic scenarios. Observed AFT ages (circles) are shown with their 2σ uncertainties and apparent exhumation rate from the slope of the weighted regression line. Predicted ages are shown with their model-derived erosion rate for the four tectonic scenarios: Slip only on the MFT (squares), equal overthrusting rate on the MFT and MCT (triangles), larger overthrusting rate on the MFT than the MCT (inverted triangles), and larger overthrusting rate on the MCT than MFT (diamonds). Abbreviations are as in Figures 1 and 2.
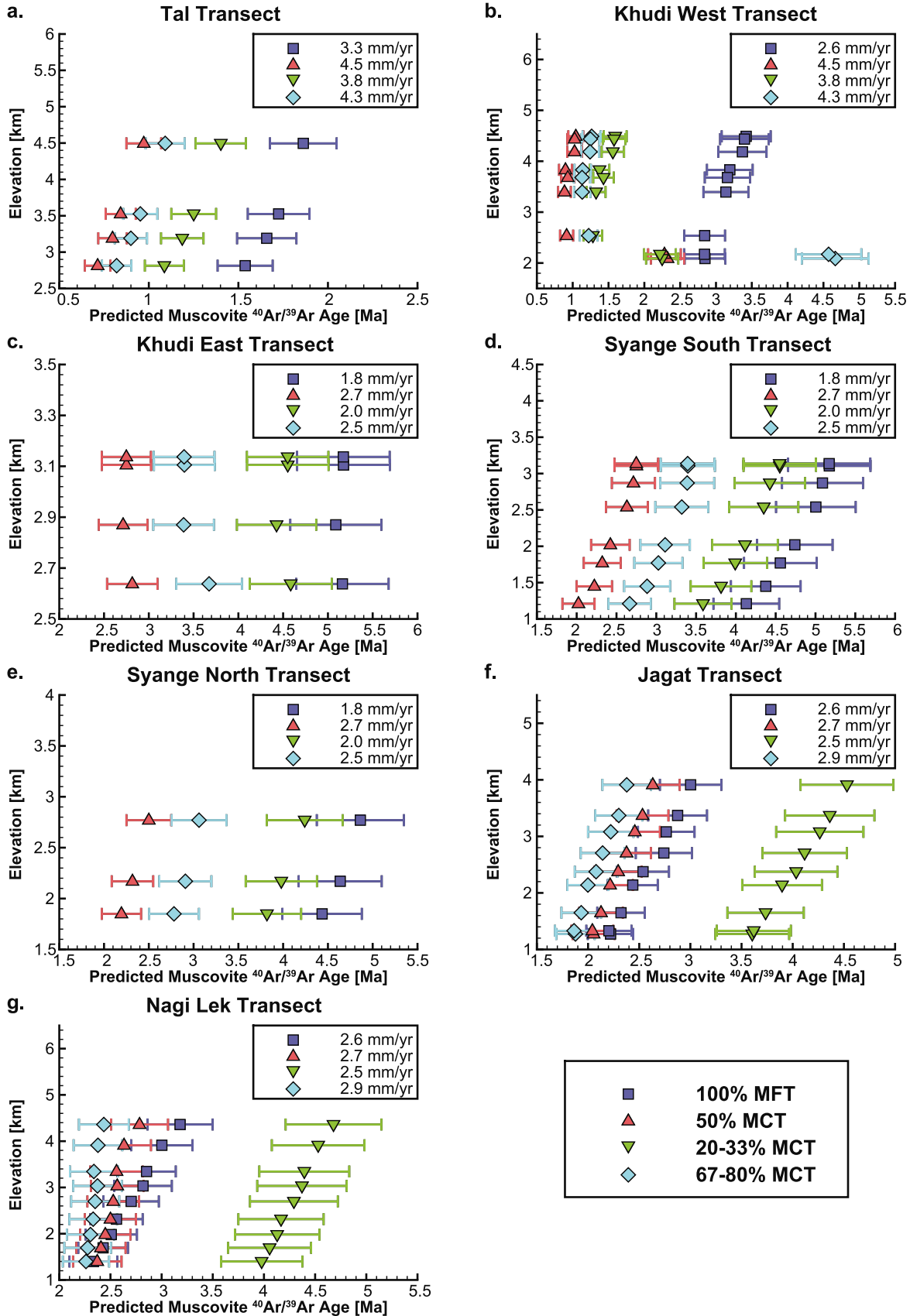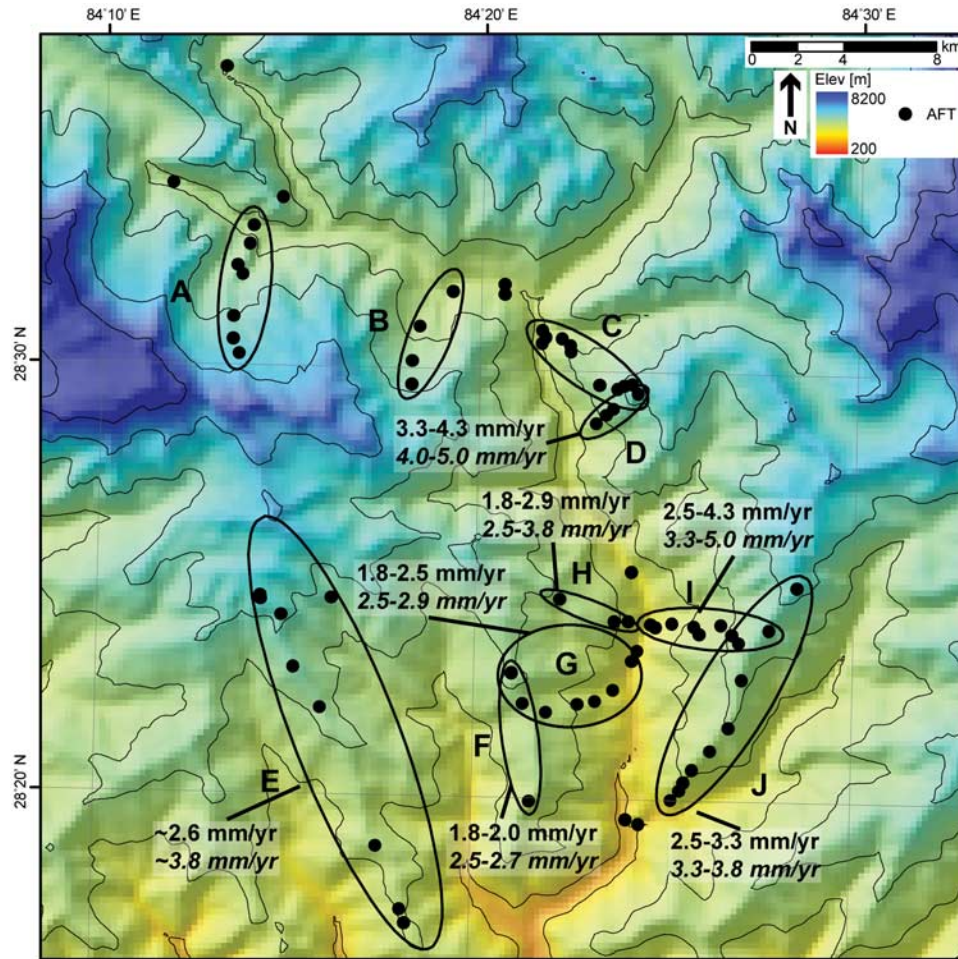
Figure 10

Figure 11. Model-constrained range of erosion rates for the data transects (ovals) shown on a shaded relief DEM of the study area with sample locations for AFT data (circles). Ranges are listed where at least 80% of the predicted ages are within the 2σ uncertainties of the observed ages. The upper range is for a model with a Greater Himalayan sequence heat production of 3.0 μW/m^3 and the lower, italicized range is for a heat production of 0.8 μW/m^3. Abbreviations are as in Figures 1 and 2, and transect names are as in Figure 2.

transects where at least 80% of the predicted AFT ages fit within the 2σ uncertainties of the observed ages. The range of erosion rates listed is from all kinematic scenarios and thermal models with a 20 mW/m^2 basal heat flux, 2.5 W/m K thermal conductivity and shear heating. The range of rates for models with GHS heat production values of 3.0 μW/m^3 and 0.8 μW/m^3 are shown beside the transects on top and bottom, respectively. The AFT data are best fit by kinematic models that produce erosion rates of 1.8–5.0 mm/yr. However, no single kinematic model can fit all of the data

transects. For example, the Khudi East transect (F in Figure 2) requires erosion rates of no greater than 2.0 mm/yr for the high heat production models, while the Tal transect (D in Figure 2) requires an erosion rate of at least 3.3 mm/yr. This suggests that the erosion rate across the Marsyandi River drainage is not only rapid, but also spatially variable.

[58] One possible explanation for the inability of the model to fit all the AFT data equally well is smaller-scale faulting within the MCT sheet. *Hodges et al.* [2004] found evidence of several faults between the MCT and STF within

Figure 10. Predicted muscovite ^{40}Ar/^{39}Ar ages in transects for different kinematic scenarios. Ages are shown with 10% age uncertainties and their model-derived erosion rate for the four tectonic scenarios: Slip only on the MFT (squares), equal overthrusting rate on the MFT and MCT (triangles), larger overthrusting rate on the MFT than the MCT (inverted triangles), and larger overthrusting rate on the MCT than the MFT (diamonds). Abbreviations are as in Figure 1.

the Marsyandi River valley with tectonically significant Quaternary displacement on them. These smaller-scale features were shown to offset the cooling ages of AFT samples from *Burbank et al.* [2003] by ∼1 Ma. The simplified the tectonic scenario in model does not reproduce the effects of displacement on the smaller-scale faults because we do not know enough about their geometry to include them. Rather, we evaluated the effects of the primary structures. Because there may be many unmapped smaller-scale faults, we contend that it is reasonable to focus on the larger-scale tectonic elements, which should have more influence on the regional cooling age patterns.

[59] Another potential explanation for the difference in rates required to fit the data transects is changes in topographic relief. A local weather network in the study area [*Barros et al.*, 2000; *Burbank et al.*, 2003] shows that annual monsoon precipitation varies from ∼0.5 to 4.0 m/yr across the Greater Himalayan zone over a 6-year period of observations. Although not observed in the data used by *Burbank et al.* [2003], it is possible that, if present-day precipitation patterns are representative of long-term precipitation patterns, precipitation could influence the spatial distribution of erosion, as suggested by numerical models [e.g., *Willett*, 1999]. *Gabet et al.* [2004] found a strong correlation between mean hillslope angles and mean annual rainfall in the Himalaya, where landsliding controls the maximum hillslope angles and relief within unglaciated valleys. They concluded that precipitation may control relief in the Himalaya and that the response time to changes in precipitation may be rapid (<10 kyr). *Hodges et al.* [2004] looked at river channel morphologies from the region spanning the southern Tibetan zone to the northern Lesser Himalayan zone and argued that deformation is coupled to precipitation in the Himalaya. They suggest that the focused precipitation along the southernmost edge of the Greater Himalayan zone has led to reactivation of the MCT, presumably driving rock uplift across the entire Greater Himalayan zone. Notably, however, our modeled erosion rates are at least as rapid for the northern transects as in the southern transects, despite a reduction of precipitation by >50%. This absence of a north-south trend in erosion rates also appears in the samples collected at river level across the study area (see *Blythe et al.* [2007, Figure 3] for sample ages and locations). A comparison of the best fit erosion rates constrained by the χ^2 misfit for the northern versus southern river bottom samples shows that the rates are statistically indistinguishable. A rate of ∼2.8 mm/yr provides the best statistical match to the entire river bottom data set, but rates as high as 4−5 mm/yr are admissible. Hence, with the exception of three more slowly eroding (and wetter) transects in the south (Khudi East, Syange South, Syange North transects; F, G, H in Figure 2), no discernable gradient in erosion rates emerges from this study.

[60] Without any change in tectonic uplift, spatial variations in erosion could lead to relatively short-lived changes in topographic relief. For example, if relief increases, cooling ages near the valley would be younger (from river incision) and ages near ridges would be older (from increased distance traveled since closure) [*Braun*, 2002].

Although relief changes can affect cooling ages, our model is unable to simulate changes in relief. All we can conclude at this time is that relief change is one possible mechanism for some of the smaller misfits observed between predicted and observed ages.

[61] It is also possible that topographically driven fluid flow may have modified the subsurface thermal field and affected the AFT ages. Groundwater can carry thermal energy from ridges to valleys as it flows, which would decrease the thermal gradient beneath peaks and increase it beneath valleys. The effect on cooling ages would be to produce older ages on ridges and younger ages in the valleys, rendering the age-elevations trends less steep. *Evans et al.* [2004] mapped several hot springs within the Marsyandi valley, showing that the groundwater may be heated by the surrounding ridges. The magnitude of this effect depends on many other factors (such as rock permeability, hillslope geometry and precipitation) and is currently unknown. Overall, we consider temporal variations in topographic relief, hydrothermal heating, slip on faults that were not modeled and unknown spatial variations in heat production and thermal conductivity to be the important possibilities for explaining the misfit of the model-predicted ages to the data. Further modeling is underway to quantify these effects.

7. Conclusions

[62] We used a 3-D coupled thermokinematic model to generate subsurface thermal fields for the Marsyandi River valley in central Nepal, from which thermochronometer ages were predicted and compared to collected data. The model is parameterized by the 3-D variability in overlying topography, fault geometry, fault kinematics, boundary conditions and material properties. The primary results of this study are as follows:

[63] 1. In regions that are rapidly exhumed, the kinematic field and associated thermal advection dominate over the influences of material properties and basal heat flux in affecting the thermal history. For example, the difference in misfit due to the different basal heat flux values is trivial compared to the kinematic influence (Figure 8). In comparing the misfits among the other material properties, we find that kinematics always dominates. Across the variation expected in natural rock samples, the influence of varying material properties is concealed by the advective heat transfer from the kinematic field.

[64] 2. The range of apparent exhumation rates derived from the slope of regression lines through sample ages versus elevation is −2.6 to 12.2 mm/yr. The range of erosion rates in the model that provide a good fit between predicted and observed AFT ages is less than half as large (1.8−5.0 mm/yr). This >200% difference between the simple 1-D interpretation using regression lines and the model-constrained rates illustrates the utility thermokinematic models for reducing the variance in calculated erosion rates. Rapid erosion, nonvertical exhumation and high-relief topography will likely invalidate the assumptions required to accurately calculate exhumation rates using the slope of

Table A1. GHS Thermal Conductivity Measurements

Sample	Formation	Lithology	Foliation-Parallel Whole Rock Conductivity, W/m K	Foliation-Perpendicular Whole Rock Conductivity, W/m K	Foliation
NP001	I	biotite-muscovite gneiss	5.0		F_1
NP002	I	biotite-muscovite gneiss	4.0		F_1
NP003	I	biotite-muscovite gneiss	4.7	2.3	F_2
NP004	I	biotite-muscovite gneiss	4.0	2.9	F_1
NP005	I	biotite-muscovite gneiss	3.2	3.0	F_1
NP006	I	biotite-muscovite gneiss	4.3		F_1
NP007	I	biotite-muscovite gneiss	3.6	2.6	F_1
NP008	I	biotite-muscovite gneiss	3.9	2.3	F_1
	I	biotite-muscovite gneiss		3.8	F_1
NP009	II	banded calc-silicate gneiss	2.4	2.0	F_1
NP010	II	banded calc-silicate gneiss	3.2		F_1
	II	banded calc-silicate gneiss	3.2		F_1
NP011	II	banded calc-silicate gneiss	4.4	2.6	F_2

regression lines through vertical transect data potentially leading to large errors.

[65] 3. The AFT data do not allow us to rule out any of the modeled kinematic scenarios and we are not able to say whether the MCT has had tectonically significant displacement since 3 Ma.

[66] 4. Differentiating between possible thrust belt kinematic models requires (1) rock exhumation pathways that are considerably different and (2) either slower exhumation rates or a thermochronometer data set that covers higher temperatures. The kinematic scenarios tested differed by only 8° in rock exhumation trajectory and the AFT data were not sensitive to this difference. We suggest that the possible rock exhumation trajectories must be considerably larger than 8° in order to have sensitivity with low-temperature thermochronometers. In areas that are exhumed at rates of less that 1 mm/yr, distances to the closure temperature for low-temperature thermochronometers may be greater and larger differences in the subsurface thermal field should exist. At these slower rates, it may be possible to differentiate more subtle differences in rock exhumation trajectories. Smaller differences in rock exhumation pathways might also be detected using higher-temperature thermochronometers (such as muscovite $^{40}Ar/^{39}Ar$) because the difference in distance traveled from the closure temperature should be larger at higher temperatures. Future studies in rapidly eroding collisional orogens may benefit from the use of these higher-temperature systems when attempting to constrain thermal and kinematic scenarios.

[67] 5. No single kinematic model can fit at least 80% of the AFT ages for all transects. This suggests that erosion in the study area is nonuniform. Possible explanations for the spatial variability are unmapped small-scale faults, relief change from differential erosion within the basin or groundwater flow affecting the cooling ages.

[68] 6. Samples should be collected on hillslopes that face the same direction as the thrust vergence when using steady state model topography. Samples collected on hillslopes that face opposite to the thrust vergence and have slope angles

similar to or greater than the fault dip angle present problems when generating predicted rock thermal histories. For slope angles that are greater than the fault dip angle, particles may be tracked out of the model domain as they move back in time parallel to the fault. Ages predicted from these thermal histories are meaningless as the thermal history is clearly unrealistic. However, samples collected in this type of orientation likely contain valuable information about the timing and rate of valley formation (e.g., Bagarchhap, Chame transects; B, A in Figure 10) and are well suited for evaluating landscape evolution models of valley incision.

Appendix A: Thermal Property Measurements

[69] Thermal conductivity was measured on 11 samples from Formations I and II in the GHS from central Nepal (Table A1) (see *Hodges* [2000] for a description of the GHS formations). The measurements were made by P. Galanis and C. Williams at the U.S. Geological Survey office in Menlo Park, California, using the technique outlined by *Sass et al.* [1984]. Samples were measured both parallel and perpendicular to the dominant foliation and a significant anisotropy was observed.

[70] Radiogenic heat-producing element concentrations were measured on 7 of the 11 samples from the GHS (Table A2). Samples were analyzed for the K, Th, and U via gamma ray spectrometry by J. Kaste and A. Heimsath at Dartmouth College in Hanover, New Hampshire. Potassium values were determined by measuring the ^{40}K emission at 1461 keV, and assuming a ^{40}K abundance of 0.01177% and ^{40}K branching ratio (e.g., gamma yield) of 10.7%. Thorium concentrations were determined by measuring the ^{228}Ac gamma ($T_{1/2}$ = ~6 hr) at 911 keV, assuming a gamma yield of 28.7% and secular equilibrium between it and ^{232}Th. ^{238}U was determined by measuring the ^{234}Th decay emission (direct daughter of ^{238}U, $T_{1/2}$ = 24 d) at 63.3 keV. ^{235}U was calculated by assuming a $^{235}U/^{238}U$ abundance of

Table A2. GHS Radiogenic Heat Production Measurements

Sample	Formation	Lithology	K, %	^{235}U, ppm	^{238}U, ppm	^{232}Th, ppm	A, μW/m^3
NP002	I	biotite-muscovite gneiss	3.26	0.016	2.161	14.893	2.0
NP004	I	biotite-muscovite gneiss	1.03	0.012	1.599	7.379	1.1
NP005	I	biotite-muscovite gneiss	3.92	0.033	4.608	18.229	3.0
NP007	I	biotite-muscovite gneiss	2.10	0.017	2.287	12.228	1.7
NP009	II	banded calc-silicate gneiss	3.34	0.024	3.269	15.259	2.4
NP010	II	banded calc-silicate gneiss	3.06	0.017	2.388	11.692	1.8
NP011	II	banded calc-silicate gneiss	4.37	0.020	2.737	17.095	2.4

0.72% (J. Kaste, personal communication, 2006). Radiogenic heat production was calculated using an equation modified from *Birch* [1954],

$$A = 0.01\rho\left(9.69\left(^{238}\mathrm{U} + {}^{235}\mathrm{U}\right) + 2.65\mathrm{Th} + 3.58\mathrm{K}\right) \quad (A1)$$

where A is the volumetric heat production in μW/m^3, ρ is the average rock density in g/cm^3, K is the potassium concentration in percent, and ^{238}U, ^{235}U, and Th are the uranium and thorium concentrations in parts per million. An average rock density of 2.8 g/cm^3 was assumed in calculating A for Table A2.

References

Arita, K. (1983), Origin of the inverted metamorphism of the Lower Himalayas, central Nepal, *Tectonophysics*, 95, 43–60.

Barros, A. P., M. Joshi, J. Putkonen, and D. W. Burbank (2000), A study of the 1999 monsoon rainfall in a mountainous region in central Nepal using TRMM products and rain gauge observations, *Geophys. Res. Lett.*, 27, 3683–3686.

Barton, C. M., and P. C. England (1979), Shear heating at the Olympos (Greece) thrust and the deformation properties of carbonates at geological strain rates, *Geol. Soc. Am. Bull.*, 90, 483–492.

Batt, G. E., and M. T. Brandon (2002), Lateral thinking: 2-D interpretation of thermochronology in convergent orogenic settings, *Tectonophysics*, 349, 185–201.

Beaumont, C., P. Fullsack, and J. Hamilton (1992), Erosional control of active compressional orogens, in *Thrust Tectonics*, edited by K. R. McClay, pp. 1–18, CRC Press, Boca Raton, Fla.

Beaumont, C., R. A. Jamieson, M. H. Nguyen, and B. Lee (2001), Himalayan tectonics explained by extrusion of a low-viscosity crustal channel coupled to focused surface denudation, *Nature*, 414, 738–742.

Bilham, R., et al. (1997), GPS measurements of present-day convergence across the Nepal Himalaya, *Nature*, 386, 61–64.

Birch, A. F. (1954), Heat from radioactivity, in *Nuclear Geology*, edited by H. Faul, pp. 148–175, John Wiley, Hoboken, N. J.

Blythe, A. E., D. W. Burbank, and J. Putkonen (2007), Plio-Quaternary exhumation history of the central Nepalese Himalaya: 1. Apatite and zircon fission-track and apatite [U-Th]/He analyses, *Tectonics*, doi:10.1029/2006TC001990, in press.

Bollinger, L., P. Henry, and J. P. Avouac (2006), Mountain building in the Nepal Himalaya: Thermal and kinematic model, *Earth Planet. Sci. Lett.*, 244, 58–71.

Braun, J. (2002), Quantifying the effect of Recent relief changes on age-elevation relationships, *Earth Planet. Sci. Lett.*, 200, 331–343.

Braun, J. (2005), Quantitative constraints on the rate of landform evolution derived from low-temperature thermochronology, in *Low-Temperature Thermochronology: Techniques, Interpretations, and Applications*, *Rev. Mineral. Geochem.*, vol. 58, edited by P. W. Reiners and T. A. Ehlers, pp. 351–374, Mineral. Soc. of Am., Washington, D. C.

Braun, J., and X. Robert (2005), Constraints on the rate of post-orogenic erosional decay from low-temperature thermochronological data; application to the Dabie Shan, China, *Earth Surf. Processes Landforms*, 30, 1203–1225.

Braun, J., and P. van der Beek (2004), Evolution of passive margin escarpments; what can we learn from low-temperature thermochronology?, *J. Geophys. Res.*, 109(F4), F04009, doi:10.1029/2004JF000147.

Brewer, I., and D. W. Burbank (2006), Thermal and kinematic modeling of bedrock and detrital cooling ages in the central Himalaya, *J. Geophys. Res.*, 111(B9), B09409, doi:10.1029/2004JB003304.

Brewer, I. D., D. W. Burbank, and K. V. Hodges (2003), Modelling detrital cooling-age populations; insights from two Himalayan catchments, *Basin Res.*, 15, 305–320.

Brewer, I. D., D. W. Burbank, and K. V. Hodges (2006), Downstream development of a detrital cooling-age signal: Insights from ^{40}Ar/^{39}Ar muscovite thermochronology in the Nepalese Himalaya, in *Tectonics, Climate, and Landscape Evolution*, edited by Sean D. Willett, *Spec. Pap. Geol. Soc. Am.*, 398, 321–338.

Brun, J.-P., J.-P. Burg, and M. Chen Guo (1985), Strain trajectories above the Main Central Thrust (Himalaya) in southern Tibet, *Nature*, 313, 388–390.

Brunel, M. (1986), Ductile thrusting in the Himalayas; shear sense criteria and stretching lineations, *Tectonics*, 5, 247–265.

Burbank, D. W., A. E. Blythe, J. Putkonen, B. Pratt-Sitaula, E. Gabet, M. Oskin, A. Barros, and T. P. Ojha (2003), Decoupling of erosion and precipitation in the Himalayas, *Nature*, 426, 652–655.

Catlos, E. J., T. M. Harrison, M. J. Kohn, M. Grove, F. J. Ryerson, C. E. Manning, and B. N. Upreti (2001), Geochronologic and thermobarometric constraints on the evolution of the Main Central Thrust, central Nepal Himalaya, *J. Geophys. Res.*, 106, 16,177–16,204.

Clauser, C., and E. Huenges (1995), Thermal conductivity of rocks and minerals, in *Rock Physics and Phase Relations: A Handbook of Physical Constants*, *Ref. Shelf*, vol. 3, edited by T. J. Aherns, pp. 105–126, AGU, Washington, D. C.

Coleman, M. E. (1998), U-Pb constraints on Oligocene-Miocene deformation and anatexis within the central Himalaya, Marsyandi Valley, Nepal, *Am. J. Sci.*, 298, 553–571.

Copeland, P., T. M. Harrison, K. V. Hodges, P. Maruejol, P. Le Fort, and A. Pecher (1991), An early Pliocene thermal disturbance of the Main Central Thrust, central Nepal; implications for Himalayan tectonics, *J. Geophys. Res.*, 96, 8475–8500.

DeCelles, P. G., D. M. Robinson, J. Quade, T. P. Ojha, C. N. Garzione, P. Copeland, and B. N. Upreti (2001), Stratigraphy, structure, and tectonic evolution of the Himalayan fold-thrust belt in western Nepal, *Tectonics*, 20, 487–509.

Dodson, M. H. (1973), Closure temperature in cooling geochronological and petrological systems, *Contrib. Mineral. Petrol.*, 40, 259–274.

Donelick, R. A., P. B. O'Sullivan, and R. A. Ketcham (2005), Apatite fission-track analysis, in *Low-Temperature Thermochronology: Techniques, Interpretations, and Applications*, *Rev. Mineral. Geochem.*, vol. 58, edited by P. W. Reiners and T. A. Ehlers, pp. 49–94, Mineral. Soc. of Am., Washington, D. C.

Edwards, R. M. (1995), ^{40}Ar/^{39}Ar geochronology of the Main Central Thrust (MCT) region: Evidence for late Miocene to Pliocene disturbances along the MCT, Marsyangdi River valley, west-central Nepal Himalaya, *J. Nepal Geol. Soc.*, 10, 41–46.

Ehlers, T. A. (2005), Crustal thermal processes and the interpretation of thermochronometer data, in *Low-Temperature Thermochronology: Techniques, Inter-*

pretations, and Applications, Rev. Mineral. Geochem., vol. 58, edited by P. W. Reiners and T. A. Ehlers, pp. 315–350, Mineral. Soc. of Am., Washington, D. C.

Ehlers, T. A., and K. A. Farley (2003), Apatite (U-Th)/He thermochronometry; methods and applications to problems in tectonic and surface processes, *Earth Planet. Sci. Lett.*, *206*, 1–14.

Ehlers, T. A., P. A. Armstrong, and D. S. Chapman (2001), Normal fault thermal regimes and the interpretation of low-temperature thermochronometers, *Phys. Earth Planet. Inter.*, *126*, 179–194.

Ehlers, T. A., S. D. Willett, P. A. Armstrong, and D. S. Chapman (2003), Exhumation of the Central Wasatch Mountains, Utah: 2. Thermo-kinematics of exhumation and thermochronometer interpretation, *J. Geophys. Res.*, *108*(B3), 2173, doi:10.1029/2001JB001723.

Ehlers, T. A., et al. (2005), Computational tools for low-temperature thremochronometer interpretation, in *Low-Temperature Thermochronology: Techniques, Interpretations, and Applications, Rev. Mineral. Geochem.*, vol. 58, edited by P. W. Reiners and T. A. Ehlers, pp. 589–622, Mineral. Soc. of Am., Washington, D. C.

England, P., P. Le Fort, P. Molnar, and A. Pecher (1992), Heat sources for Tertiary metamorphism and anatexis in the Annapurna-Manaslu region, central Nepal, *J. Geophys. Res.*, *97*, 2107–2128.

Evans, M. J., L. A. Derry, and C. France-Lanord (2004), Geothermal fluxes of alkalinity in the Narayani river system of central Nepal, *Geochem. Geophys. Geosyst.*, *5*, Q08011, doi:10.1029/2004GC000719.

Gabet, E. J., B. A. Pratt-Sitaula, and D. W. Burbank (2004), Climatic controls on hillslope angle and relief in the Himalayas, *Geology*, *32*, 629–632.

Gansser, A. (1964), *Geology of the Himalayas*, 289 pp., Wiley Interscience, Hoboken, N. J.

Graham, C. M., and P. C. England (1976), Thermal regimes and regional metamorphism in the vicinity of overthrust faults; an example of shear heating and inverted metamorphic zonation from southern California, *Earth Planet. Sci. Lett.*, *31*, 142–152.

Grujic, D., M. Casey, C. Davidson, L. S. Hollister, R. Kuendig, T. L. Pavlis, and S. M. Schmid (1996), Ductile extrusion of the Higher Himalayan crystalline in Bhutan; evidence from quartz microfabrics, *Tectonophysics*, *260*, 21–43.

Gupta, A. K., and E. Thomas (2003), Initiation of Northern Hemisphere glaciation and strengthening of the Northeast Indian monsoon; Ocean Drilling Program Site 758, eastern equatorial Indian Ocean, *Geology*, *31*, 47–50.

Gupta, S. (1997), Himalayan drainage patterns and the origin of fluvial megafans in the Ganges foreland basin, *Geology*, *25*, 11–14.

Hames, W. E., and S. A. Bowring (1994), An empirical evaluation of the argon diffusion geometry in muscovite, *Earth Planet. Sci. Lett.*, *124*, 161–169.

Hansen, F. D., and N. L. Carter (1982), Creep of selected crustal rocks at 1000 MPa, *Eos Trans. AGU*, *63*, 437.

Harrison, T. M., and P. K. Zeitler (2005), Fundamentals of Noble Gas Thermochronometry, in *Low-Temperature Thermochronology: Techniques, Interpretations, and Applications, Rev. Mineral. Geochem.*, vol. 58, edited by P. W. Reiners and T. A. Ehlers, pp. 123–149, Mineral. Soc. of Am., Washington, D. C.

Harrison, T. M., P. Copeland, W. S. F. Kidd, and A. Yin (1992), Raising Tibet, *Science*, *255*, 1663–1670.

Harrison, T. M., F. J. Ryerson, P. Le Fort, A. Yin, O. M. Lovera, and E. J. Catlos (1997), A late Miocene-Pliocene origin for the central Himalayan inverted metamorphism, *Earth Planet. Sci. Lett.*, *146*, E1–E7.

Henry, P., X. Le Pichon, and B. Goffe (1997), Kinematic, thermal and petrological model of the Himalayas; constraints related to metamorphism within the underthrust Indian crust and topographic elevation, *Tectonophysics*, *273*, 31–56.

Hodges, K. V. (2000), Tectonics of the Himalaya and southern Tibet from two perspectives, *Geol. Soc. Am. Bull.*, *112*, 324–350.

Hodges, K. V., R. R. Parrish, and M. P. Searle (1996), Tectonic evolution of the central Annapurna Range, Nepalese Himalayas, *Tectonics*, *15*, 1264–1291.

Hodges, K. V., J. M. Hurtado, and K. X. Whipple (2001), Southward extrusion of Tibetan crust and its effect on Himalayan tectonics, *Tectonics*, *20*, 799–809.

Hodges, K. V., C. W. Wobus, K. Ruhl, T. Schildgen, and K. X. Whipple (2004), Quaternary deformation, river steepening, and heavy precipitation at the front of the Higher Himalayan ranges, *Earth Planet. Sci. Lett.*, *220*, 379–389.

Hubbard, M. S., and T. M. Harrison (1989), $^{40}Ar/^{39}Ar$ age constraints on deformation and metamorphism in the Main Central Thrust zone and Tibetan Slab, eastern Nepal Himalaya, *Tectonics*, *8*, 865–880.

Huntington, K. W., and K. V. Hodges (2006), A comparative study of detrital mineral and bedrock age-elevation methods for estimating erosion rates, *J. Geophys. Res.*, *111*, F03011, doi:10.1029/2005JF000454.

Huntington, K. W., A. E. Blythe, and K. V. Hodges (2006), Climate change and Late Pliocene acceleration of erosion in the Himalaya, *Earth Planet. Sci. Lett.*, *252*, 107–118.

Jouanne, F., J. L. Mugnier, J. F. Gamond, P. Le Fort, M. R. Pandey, L. Bollinger, M. Flouzat, and J. P. Avouac (2004), Current shortening across the Himalays of Nepal, *Geophys. J. Int.*, *157*, 1–14.

Kohl, T., and R. J. Hopkirk (1995), "FRACTure" a simulation code for forced fluid flow and transport in fractured, porous rock, *Geothermics*, *24*, 333–343.

Larson, K. M., R. Buergmann, R. Bilham, and J. T. Freymueller (1999), Kinematics of the India-Eurasia collision zone from GPS measurements, *J. Geophys. Res.*, *104*, 1077–1093.

Laslett, G. M., P. F. Green, I. R. Duddy, and A. J. W. Gleadow (1987), Thermal annealing of fission tracks in apatite, *Chem. Geol.*, *65*, 1–13.

Lavé, J., and J. P. Avouac (2000), Active folding of fluvial terraces across the Siwaliks Hills, Himalays of central Nepal, *J. Geophys. Res.*, *105*, 5735–5770.

Le Fort, P. (1975), Himalayas; the collided range: Present knowledge of the continental arc, *Am. J. Sci.*, *275-A*, 1–44.

Lyon-Caen, H., and P. Molnar (1983), Constraints on the structure of the Himalaya from an analysis of gravity anomalies and a flexural model of the lithosphere, *J. Geophys. Res.*, *88*, 8171–8191.

Macfarlane, A. M. (1993), Chronology of tectonic events in the crystalline core of the Himalaya, Langtang National Park, central Nepal, *Tectonics*, *12*, 1004–1025.

Macfarlane, A. M., K. V. Hodges, and D. Lux (1992), A structural analysis of the Main Central Thrust zone, Langtang National Park, central Nepal Himalaya, *Geol. Soc. Am. Bull.*, *104*, 1389–1402.

Mancktelow, N. S., and B. Grasemann (1997), Time-dependent effects of heat advection and topography on cooling histories during erosion, *Tectonophysics*, *270*, 167–195.

Molnar, P., P. England, and J. Martinod (1993), Mantle dynamics, uplift of the Tibetan Plateau, and the Indian monsoon, *Rev. Geophys.*, *31*, 357–396.

Niemi, N. A., M. Oskin, D. W. Burbank, A. M. Heimsath, and E. J. Gabet (2005), Effects of bedrock landslides on cosmogenically determined erosion rates, *Earth Planet. Sci. Lett.*, *237*, 480–498.

Pandey, M. R., R. P. Tandukar, J. P. Avouac, J. Lave, and J. P. Massot (1995), Interseismic strain accumulation on the Himalayan crustal ramp (Nepal), *Geophys. Res. Lett.*, *22*, 751–754.

Pearson, O. N., and P. G. DeCelles (2005), Structural geology and regional tectonic significance of the Ramgarh thrust, Himalayan fold-thrust belt of Nepal, *Tectonics*, *24*, TC4008, doi:10.1029/2003TC001617.

Raymo, M. E. (1994), The initiation of Northern Hemisphere glaciation, *Annu. Rev. Earth Planet. Sci.*, *22*, 353–383.

Reiners, P. W., T. A. Ehlers, S. G. Mitchell, and D. R. Montgomery (2003), Coupled spatial variations in precipitation and long-term erosion rates across the Washington Cascades, *Nature*, *426*, 645–647.

Ring, U., M. T. Brandon, S. D. Willett, and G. S. Lister (1999), Exhumation processes, in *Exhumation Processes: Normal Faulting, Ductile Flow and Erosion*, edited by U. Ring et al., *Geol. Soc. Spec. Publ.*, *154*, 1–27.

Robbins, G. A. (1972), Radiogenic argon diffusion in muscovite under hydrothermal conditions, thesis or dissertation, Master's, monographic thesis, Brown Univ., Providence, R. I.

Robinson, D. M., P. G. DeCelles, C. N. Garzione, O. N. Pearson, T. M. Harrison, and E. J. Catlos (2003), Kinematic model for the Main Central Thrust in Nepal, *Geology*, *31*, 359–362.

Roy, S., and R. U. M. Rao (2000), Heat flow in the Indian Shield, *J. Geophys. Res.*, *105*, 25,587–25,604.

Ruddiman, W. F., M. E. Raymo, W. L. Prell, and J. E. Kutzbach (1997), The uplift-climate connection; a synthesis, in *Global Tectonics and Climate Change*, edited by W. F. Ruddiman, and W. Prell, pp. 471–515, Springer, New York.

Ruhl, K. W., and K. V. Hodges (2005), The use of detrital mineral cooling ages to evaluate steady state assumptions in active orogens: An example from the central Nepalese Himalaya, *Tectonics*, *24*, TC4015, doi:10.1029/2004TC001712.

Rybach, L. (1976), Radioactive heat production; a physical property determined by the chemistry of rocks, in *The Physics and Chemistry of Minerals and Rocks*, edited by R. G. J. Strens, pp. 309–318, John Wiley, Hoboken, N. J.

Sass, J. H., J. P. Kennelly Jr., E. P. Smith, and W. E. Wendt (1984), Laboratory line-source methods for the measurement of thermal conductivity of rocks near room temperature, *U.S. Geol. Surv. Open File Rep.*, *84-91*, 21 pp.

Sass, J. H., A. H. Lachenbruch, T. H. Moses Jr., P. Morgan, M. D. Zoback, and A. H. Lachenbruch (1992), Heat flow from a scientific research well at Cajon Pass, California, *J. Geophys. Res.*, *97*, 5017–5030.

Schelling, D., and K. Arita (1991), Thrust tectonics, crustal shortening, and the structure of the far-eastern Nepal Himalaya, *Tectonics*, *10*, 851–862.

Searle, M. P. (1999), Extensional and compressional faults in the Everest-Lhotse Massif, Khumbu Himalaya, Nepal, *J. Geol. Soc. London*, *156*, 227–240.

Searle, M. P., and L. Godin (2003), The South Tibetan detachment and the Manaslu Leucogranite: A structural reinterpretation and restoration of the Annapurna-Manaslu Himalaya, Nepal, *J. Geol.*, *111*, 505–523.

Seeber, L., and V. Gornitz (1983), River profiles along the Himalayan Arc as indicators of active tectonics, *Tectonophysics*, *92*, 335–367.

Stüwe, K., L. White, and R. Brown (1994), The influence of eroding topography on steady-state isotherms; application to fission track analysis, *Earth Planet. Sci. Lett.*, *124*, 63–74.

Suppe, J. (1983), Geometry and kinematics of fault-bend folding, *Am. J. Sci.*, *283*, 684–721.

Tagami, T., and P. B. O'Sullivan (2005), Fundamentals of fission-track thermochronology, in *Low-Temperature Thermochronology: Techniques, Interpretations, and Applications, Rev. Mineral. Geochem.*, vol. 58, edited by P. W. Reiners and T. A. Ehlers, pp. 19–47, Mineral. Soc. of Am., Washington, D. C.

Tapponnier, P., Z. Xu, F. Roger, B. Meyer, N. Arnaud, G. Wittlinger, and J. Yang (2001), Oblique stepwise rise and growth of the Tibet Plateau, *Science*, *294*, 1671–1677.

Thiede, R. C., B. Bookhagen, R. Arrowsmith, E. R. Sobel, and M. R. Strecker (2004), Climatic control on rapid exhumation along the southern Himalayan Front, *Earth Planet. Sci. Lett.*, *222*, 791–806.

Thiede, R. C., J. R. Arrowsmith, B. Bookhagen, M. O. McWilliams, E. R. Sobel, and M. R. Strecker (2005), From tectonically to erosionally controlled

development of the Himalayan Orogen, *Geology*, *33*, 689–692.

Valdiya, K. S. (1980), The two intracrustal boundary thrusts of the Himalaya, *Tectonophysics*, *66*, 323–348.

Vance, D., M. Bickle, S. Ivy-Ochs, and P. W. Kubik (2003), Erosion and exhumation in the Himalaya from cosmogenic isotope inventories of river sediments, *Earth Planet. Sci. Lett.*, *206*, 273–288.

van der Beek, P., M. A. Summerfield, J. Braun, R. W. Brown, and A. Fleming (2002), Modeling post-breakup landscape development and denudational history across the southeast African (Drakensberg Escarpment) margin, *J. Geophys. Res.*, *107*(B12), 2351, doi:10.1029/2001JB000744.

Wagner, G. A., and G. M. Reimer (1972), Fission track tectonics; the tectonic interpretation of fission track apatite ages, *Earth Planet. Sci. Lett.*, *14*, 263–268.

Wagner, G. A., G. M. Reimer, and E. Jager (1977), Cooling ages derived by apatite fission-track, mica Rb-Sr and K-Ar dating: The uplift and cooling history of the Central Alps, *Mem. Ist. Geol. Min. Univ. Padova*, *XXX*.

Wang, Q., et al. (2001), Present-day crustal deformation in China constrained by Global Positioning System measurements, *Science*, *294*, 574–577.

Willett, S. D. (1999), Orogeny and orography; the effects of erosion on the structure of mountain belts, *J. Geophys. Res.*, *104*, 28,957–28,982.

Wobus, C. W., K. V. Hodges, and K. X. Whipple (2003), Has focused denudation sustained active thrusting at the Himalayan topographic front?, *Geology*, *31*, 861–864.

Wobus, C. W., A. Heimsath, K. X. Whipple, and K. V. Hodges (2005), Active out-of-sequence thrust faulting in the central Nepalese Himalaya, *Nature*, *434*, 1008–1011.

Zhang, P., P. Molnar, and W. R. Downs (2001), Increased sedimentation rates and grain sizes 2–4 Myr ago due to the influence of climate change on erosion rates, *Nature*, *410*, 891–897.

Zhang, P., Z. Shen, M. Wang, W. Gan, R. Buergmann, P. Molnar, Q. Wang, Z. Niu, J. Sun, J. Wu, H. Sun, and X. You (2004), Continuous deformation of the Tibetan Plateau from Global Positioning System data, *Geology*, *32*, 809–812.

A. E. Blythe, Geology Department, Occidental College, 1600 Campus Rd., Los Angeles, CA 90041, USA. (ablythe@oxy.edu)

D. W. Burbank, Department of Earth Science, University of California, Santa Barbara, Santa Barbara, CA 93106, USA.

T. A. Ehlers and D. M. Whipp Jr., Department of Geological Sciences, University of Michigan, Ann Arbor, MI 48109-1005, USA. (dwhipp@umich.edu)

K. V. Hodges, School of Earth and Space Exploration, Arizona State University, P.O. Box 871404, Tempe, AZ 85287-1404, USA.

K. W. Huntington, Division of Geological and Planetary Sciences, California Institute of Technology, GPS MC 100-23, 1200 E. California Blvd., Pasadena, CA 91125-0000, USA.